INTERNATIONAL JOURNAL FOR NUMERICAL METHODS IN FLUIDS
Int. J. Numer. Meth. Fluids (2010)
Published online in Wiley Online Library (wileyonlinelibrary.com). DOI: 10.1002/fld.2485

Depth-integrated, non-hydrostatic model with grid nesting for tsunami generation, propagation, and run-up

Yoshiki Yamazaki[1], Kwok Fai Cheung[1,*,†] and Zygmunt Kowalik[2]

[1]*Department of Ocean and Resources Engineering, University of Hawaii at Manoa, Honolulu, HI 96822, U.S.A.*
[2]*Institute of Marine Science, University of Alaska, Fairbanks, AK 99775, U.S.A.*

SUMMARY

Tsunamis generated by earthquakes involve physical processes of different temporal and spatial scales that extend across the ocean to the shore. This paper presents a shock-capturing dispersive wave model in the spherical coordinate system for basin-wide evolution and coastal run-up of tsunamis and discusses the implementation of a two-way grid-nesting scheme to describe the wave dynamics at resolution compatible to the physical processes. The depth-integrated model describes dispersive waves through the non-hydrostatic pressure and vertical velocity, which also account for tsunami generation from dynamic seafloor deformation. The semi-implicit, finite difference model captures flow discontinuities associated with bores or hydraulic jumps through the momentum-conserved advection scheme with an upwind flux approximation. The two-way grid-nesting scheme utilizes the Dirichlet condition of the non-hydrostatic pressure and both the horizontal velocity and surface elevation at the inter-grid boundary to ensure propagation of dispersive waves and discontinuities across computational grids of different resolution. The inter-grid boundary can adapt to bathymetric features to model nearshore wave transformation processes at optimal resolution and computational efficiency. A coordinate transformation enables application of the model to small geographic regions or laboratory experiments with a Cartesian grid. A depth-dependent Gaussian function smoothes localized bottom features in relation to the water depth while retaining the bathymetry important for modeling of tsunami transformation and run-up. Numerical experiments of solitary wave propagation and N-wave run-up verify the implementation of the grid-nesting scheme. The 2009 Samoa Tsunami provides a case study to confirm the validity and effectiveness of the modeling approach for tsunami research and impact assessment. Copyright © 2010 John Wiley & Sons, Ltd.

Received 17 June 2010; Revised 14 September 2010; Accepted 10 October 2010

KEY WORDS: non-hydrostatic pressure; dispersive waves; two-way grid-nesting scheme; run-up; dynamic seafloor deformation; 2009 Samoa Tsunami

1. INTRODUCTION

Tsunamis generated by earthquakes are commonly modeled as non-dispersive long waves with a spherical coordinate system for their propagation around the globe [1–4]. Nonlinear shallow-water models based on the finite difference method can describe basin-wide evolution and coastal run-up of tsunamis through a series of nested grids [5–8]. These explicit schemes, which provide efficient solutions to large computational problems, have become an indispensable tool for flood hazard mapping and assessment. Consistent with the shallow-water approach, the initial tsunami wave assumes the vertical component of the seafloor deformation due to earthquake rupture [9]. This static initial condition in lieu of the tsunami generation mechanism provides a practical method

*Correspondence to: Kwok Fai Cheung, Department of Ocean and Resources Engineering, University of Hawaii at Manoa, HI 96822, U.S.A.
†E-mail: cheung@hawaii.edu

for modeling of real-field tsunamis. Recent studies, however, suggest that wave dispersion and breaking as well as dynamic seafloor deformation could have non-negligible effects on the tsunami evolution and run-up processes [10–13].

The nonlinear shallow-water equations are hydrostatic and unable to describe wave dispersion. Although tsunamis are primarily shallow-water waves, dispersive effects might become important for basin-wide propagation and nearshore transformation. Through a classical Boussinesq model, Horrillo *et al.* [11] showed that wave dispersion in tsunami propagation results in a sequence of trailing waves that have significant effects on coastal run-up. The solitary wave experiment of Brigg *et al*. [14] and the tsunami measurements of Bricker *et al*. [15] reveal intricate dispersive wave patterns on the leeside of islands that cannot be reproduced by nonlinear shallow-water models. Boussinesq-type models, however, involve a complex equation system with high-order dispersion terms that might not be amenable to the grid-nesting schemes used in tsunami modeling [5–8]. In contrast, Stelling and Zijlema [16] proposed an alternate depth-integrated formulation, which introduces non-hydrostatic pressure and vertical velocity terms in the nonlinear shallow-water equations to describe weakly dispersive waves. The dispersion terms involve only first-order derivatives of the non-hydrostatic pressure that can be resolved by a low-order scheme. These semi-implicit finite-difference models produce comparable or better results in comparison to Boussinesq-type models [16, 17] and have the potential to describe basin-wide evolution as well as coastal run-up of tsunamis through a grid-nesting scheme.

The commonly used finite difference schemes in the solution of the nonlinear shallow-water equations are non-conservative leading to volume loss and energy dissipation as the wave steepness increases and the flow approaches discontinuous. This turns out to be a crucial modeling issue when tsunami bores develop nearshore and the results become grid-size dependent. Excessive energy dissipation and volume loss lead to underestimation of the flow and run-up with unintended consequences in tsunami hazard assessment. The finite volume method based on the conservative form of the nonlinear shallow-water equations captures flow discontinuities and conserves flow volume through a Godunov-type scheme involving a Riemann solver [12, 18–20]. This approach approximates breaking waves as bores or hydraulic jumps through conservation of momentum and accounts for energy dissipation across flow discontinuities without the use of empirical relations. Stelling and Duinmeijer [21] developed an equivalent shock-capturing scheme for finite difference models based on the nonlinear shallow-water equations. This momentum-conserved advection scheme, which is derived from the conservative formulation of the momentum equations, produces comparable results as a Riemann solver in shallow-water flows. Zijlema and Stelling [22] and Yamazaki *et al.* [17], respectively, applied the momentum-conserved advection scheme in a two-layer and a depth-integrated non-hydrostatic model for breaking of dispersive waves with encouraging results.

Recent advances in seismic inverse algorithms [23, 24] enable accurate descriptions of rise time and rupture propagation over the source area. This provides time series of the seafloor vertical displacement and velocity that constitute the bottom boundary condition of a non-hydrostatic model for transfer of kinetic and potential energy to the water. It is timely to implement a dispersive and shock-capturing model for better description of the physics in tsunami generation, propagation, and run-up. This involves reformulation of the depth-integrated non-hydrostatic model of Yamazaki *et al.* [17] in the spherical coordinate system with dynamic seafloor deformation and implementation of a two-way grid-nesting scheme, which can conform to topographic features for efficient computation of tsunami propagation and coastal run-up. Numerical modeling of solitary wave propagation in a channel and N-wave run-up in the Monai Valley laboratory experiment [25] provides verification of the grid-nesting scheme. However, dispersive wave models based on non-hydrostatic or Boussinesq-type formulations are prone to instabilities created by localized, steep bottom gradients [11, 26]. We propose a depth-dependent Gaussian function for smoothing of bathymetric features smaller than the water depth to improve stability and convergence of the semi-implicit, non-hydrostatic solution. The 2009 Samoa Islands Tsunami, with advanced source mechanisms and well-recorded water-level and run-up data, provides a test case to validate and demonstrate the proposed modeling approach for real-field events.

DOI: 10.1002/fld

2. DEPTH-INTEGRATED NON-HYDROSTATIC MODEL

This section reformulates the depth-integrated, non-hydrostatic model of Yamazaki *et al.* [17] in the spherical coordinate system for basin-wide tsunami propagation. The vertical velocity associated with the non-hydrostatic pressure allows implementation of a movable seafloor boundary condition to model tsunami generation. The finite difference scheme utilizes an upwind flux approximation [17, 27, 28] in the discretization of the governing equations and enforces momentum conservation in the numerical scheme to capture flow discontinuities associated with bores and hydraulic jumps.

2.1. Theoretical formulation

The boundary-value problem is defined by a spherical coordinates system (λ, ϕ, z), in which λ is longitude, ϕ is latitude, and z denotes the normal distance from the ocean surface. The governing equations for the depth-integrated, non-hydrostatic flow are derived from the incompressible Navier–Stokes equations and the continuity equation in the form:

$$\frac{\partial u}{\partial t}+\frac{u}{R\cos\phi}\frac{\partial u}{\partial \lambda}+\frac{v}{R}\frac{\partial u}{\partial \phi}+w\frac{\partial u}{\partial z}-\left(2\Omega+\frac{u}{R\cos\phi}\right)(v\sin\phi-w\cos\phi)=-\frac{1}{\rho R\cos\phi}\frac{\partial p}{\partial \lambda}+A_\lambda \quad (1)$$

$$\frac{\partial v}{\partial t}+\frac{u}{R\cos\phi}\frac{\partial v}{\partial \lambda}+\frac{v}{R}\frac{\partial v}{\partial \phi}+w\frac{\partial v}{\partial z}+\frac{wv}{R}+\left(2\Omega+\frac{u}{R\cos\phi}\right)u\sin\phi=-\frac{1}{\rho R}\frac{\partial p}{\partial \phi}+A_\phi \quad (2)$$

$$\frac{\partial w}{\partial t}+\frac{u}{R\cos\phi}\frac{\partial w}{\partial \lambda}+\frac{v}{R}\frac{\partial w}{\partial \phi}+w\frac{\partial w}{\partial z}-\frac{v^2}{R}-\left(2\Omega+\frac{u}{R\cos\phi}\right)u\cos\phi=-\frac{1}{\rho}\frac{\partial p}{\partial z}+A_z-g \quad (3)$$

$$\frac{1}{R\cos\phi}\frac{\partial u}{\partial \lambda}+\frac{1}{R\cos\phi}\frac{\partial(v\cos\phi)}{\partial \phi}+\frac{\partial w}{\partial z}=0 \quad (4)$$

where R is the earth's radius; (u, v, w) is flow velocity; t is time; Ω is the earth's angular velocity; ρ is water density; p is pressure; g is gravitational acceleration; and (A_λ, A_ϕ, A_z) is the viscous force [3, 29].

Figure 1 provides a schematic of the free-surface flow generated by seafloor deformation. The boundary conditions at the free surface and seafloor facilitate the formulation of the depth-integrated governing equations. The flow depth is the distance between the two boundaries defined as

$$D=\zeta+(h-\eta) \quad (5)$$

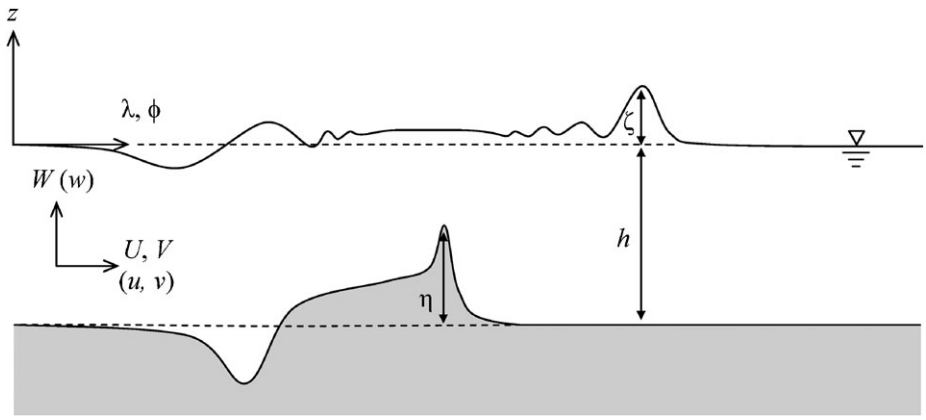

Figure 1. Schematic of free-surface flow generated by seafloor deformation.

DOI: 10.1002/fld

where ζ is the surface elevation from the still-water level, h is the water depth, and η is the seafloor displacement. Material derivatives of the surface elevation and water depth give rise to the kinematic free surface and seafloor boundary conditions as

$$w=\frac{\partial\zeta}{\partial t}+\frac{u}{R\cos\phi}\frac{\partial\zeta}{\partial\lambda}+\frac{v}{R}\frac{\partial\zeta}{\partial\phi}\quad\text{at } z=\zeta \tag{6}$$

$$w=\frac{\partial\eta}{\partial t}-\frac{u}{R\cos\phi}\frac{\partial(h-\eta)}{\partial\lambda}-\frac{v}{R}\frac{\partial(h-\eta)}{\partial\phi}\quad\text{at } z=-h+\eta \tag{7}$$

The vertical velocity w varies linearly from the seafloor to the free surface for modeling of weakly dispersive waves in depth-integrated flows. Following Casulli [30], the pressure is decomposed into hydrostatic and non-hydrostatic components as

$$p=\rho g(\zeta-z)+\rho q \tag{8}$$

where q denotes the non-hydrostatic pressure. Both the hydrostatic and non-hydrostatic pressure terms vanish at $z=\zeta$ to provide the dynamic free surface boundary condition.

Depth integration of (1), (2), and (4) and linearization of (3) taking into account the boundary conditions (6) and (7) and the pressure decomposition (8), give rise to the depth-integrated, non-hydrostatic governing equations in the spherical coordinates. The resulting λ, ϕ, and z momentum equations as well as the continuity equation are

$$\begin{aligned}&\frac{\partial U}{\partial t}+\frac{U}{R\cos\phi}\frac{\partial U}{\partial\lambda}+\frac{V}{R}\frac{\partial U}{\partial\phi}-\left(2\Omega+\frac{U}{R\cos\phi}\right)V\sin\phi\\&\quad=-\frac{g}{R\cos\phi}\frac{\partial\zeta}{\partial\lambda}-\frac{1}{2}\frac{1}{R\cos\phi}\frac{\partial q}{\partial\lambda}-\frac{1}{2}\frac{q}{DR\cos\phi}\frac{\partial(\zeta-h+\eta)}{\partial\lambda}-n^2\frac{g}{D^{1/3}}\frac{U\sqrt{U^2+V^2}}{D}\end{aligned} \tag{9}$$

$$\begin{aligned}&\frac{\partial V}{\partial t}+\frac{U}{R\cos\phi}\frac{\partial V}{\partial\lambda}+\frac{V}{R}\frac{\partial V}{\partial\phi}+\left(2\Omega+\frac{U}{R\cos\phi}\right)U\sin\phi\\&\quad=-\frac{g}{R}\frac{\partial\zeta}{\partial\phi}-\frac{1}{2}\frac{1}{R}\frac{\partial q}{\partial\phi}-\frac{1}{2}\frac{q}{DR}\frac{\partial(\zeta-h+\eta)}{\partial\phi}-n^2\frac{g}{D^{1/3}}\frac{V\sqrt{U^2+V^2}}{D}\end{aligned} \tag{10}$$

$$\frac{\partial W}{\partial t}=\frac{q}{D} \tag{11}$$

$$\frac{\partial(\zeta-\eta)}{\partial t}+\frac{1}{R\cos\phi}\frac{\partial(UD)}{\partial\lambda}+\frac{1}{R\cos\phi}\frac{\partial(V\cos\phi D)}{\partial\phi}=0 \tag{12}$$

where U, V, and W are depth-averaged velocity components in the λ, ϕ, and z directions; q is now defined as the non-hydrostatic pressure at the seafloor; and n is Manning's coefficient accounting for the surface roughness. Because of the assumption of a linear distribution, the velocity component W is simply the average value of w at the free surface and the seafloor given, respectively, by (6) and (7).

2.2. Numerical formulation

The numerical formulation includes the solution schemes for the hydrostatic and non-hydrostatic components of the governing equations as well as the coordinate transformation from spherical to Cartesian grids. Figure 2 shows the space-staggered grid for the computation. The model calculates the horizontal velocity components U and V at the cell interface and the free surface elevation ζ, the non-hydrostatic pressure q, and the vertical velocity W at the cell center, where the water depth h is defined.

Integration of the continuity equation (4) provides an update of the surface elevation at the center of cell (j,k) in terms of the fluxes, *FLX* and *FLY* along the longitude and latitude, at the

DOI: 10.1002/fld

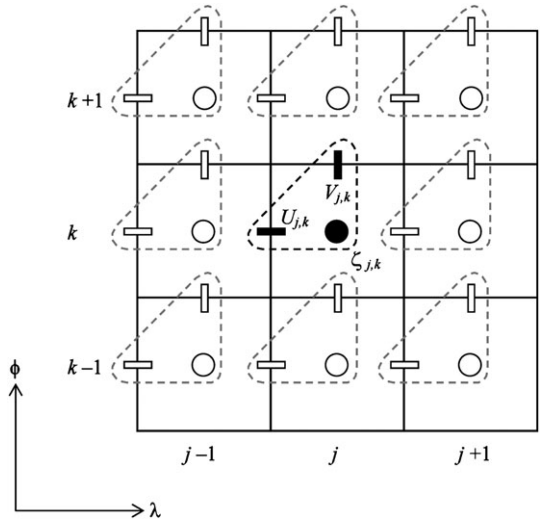

Figure 2. Definition sketch of the discretization scheme.

cell interfaces as

$$\zeta_{j,k}^{m+1} = \zeta_{j,k}^{m} + (\eta_{j,k}^{m+1} - \eta_{j,k}^{m}) - \Delta t \frac{FLX_{j+1,k} - FLX_{j,k}}{R\Delta\lambda\cos\phi_k}$$

$$= \Delta t \frac{FLY_{j,k}\cos(\phi_k + \Delta\phi/2) - FLY_{j,k-1}\cos(\phi_{k-1} + \Delta\phi/2)}{R\Delta\phi\cos\phi_k} \tag{13}$$

where m denotes the time step, Δt the time step size, and $\Delta\lambda$ and $\Delta\phi$ the respective grid sizes. The flux terms at (j,k) are estimated using the upwind flux approximation of Mader [27] as

$$FLX_{j,k} = U_p^{m+1}\zeta_{j-1,k}^{m} + U_n^{m+1}\zeta_{j,k}^{m} + U_{j,k}^{m+1}\frac{(h_{j-1,k} - \eta_{j-1,k}^{m}) + (h_{j,k} - \eta_{j,k}^{m})}{2} \tag{14a}$$

$$FLY_{j,k} = V_p^{m+1}\zeta_{j,k}^{m} + V_n^{m+1}\zeta_{j,k+1}^{m} + V_{j,k}^{m+1}\frac{(h_{j,k} - \eta_{j,k}^{m}) + (h_{j,k+1} - \eta_{j,k+1}^{m})}{2} \tag{14b}$$

in which

$$U_p^m = \frac{U_{j,k}^m + |U_{j,k}^m|}{2}, \quad U_n^m = \frac{U_{j,k}^m - |U_{j,k}^m|}{2}; \quad V_p^m = \frac{V_{j,k}^m + |V_{j,k}^m|}{2}, \quad V_n^m = \frac{V_{j,k}^m - |V_{j,k}^m|}{2} \tag{15}$$

The upwind flux approximation (14) extrapolates the surface elevation from the upwind cell, while the water depth takes on the average value from the two adjacent cells. The horizontal momentum equations provide the velocity components U and V at $(m+1)$ in (14) for the update of the surface elevation in (13). Integration of the momentum equations (9) and (10) is performed in two steps. With the non-hydrostatic terms omitted, an explicit hydrostatic solution is given by

$$\tilde{U}_{j,k}^{m+1} = U_{j,k}^m - \frac{g\Delta t}{R\Delta\lambda\cos\phi_k}(\zeta_{j,k}^m - \zeta_{j-1,k}^m) + \Delta t\left(2\Omega + \frac{U_{j,k}^m}{R\cos\phi_k}\right)\bar{V}_{x_{j,k}}^m\sin\phi_k$$

$$- \frac{\Delta t}{R\Delta\lambda\cos\phi_k}U_p^m(U_{j,k}^m - U_{j-1,k}^m) - \frac{\Delta t}{R\Delta\lambda\cos\phi_k}U_n^m(U_{j+1,k}^m - U_{j,k}^m)$$

$$- \frac{\Delta t}{R\Delta\phi}\bar{V}_{x_p}^m(U_{j,k}^m - U_{j,k-1}^m) - \frac{\Delta t}{R\Delta\phi}\bar{V}_{x_n}^m(U_{j,k+1}^m - U_{j,k}^m) - n^2 g\frac{\Delta t U_{j,k}^m\sqrt{(U_{j,k}^m)^2 + (\bar{V}_{x_{j,k}}^m)^2}}{(D_{j-1,k}^m + D_{j,k}^m)^{\frac{4}{3}}} \tag{16}$$

DOI: 10.1002/fld

$$\tilde{V}_{j,k}^{m+1} = V_{j,k}^{m} - \frac{g\Delta t}{R\Delta\phi}(\zeta_{j,k+1}^{m} - \zeta_{j,k}^{m}) - \Delta t\left(2\Omega + \frac{\bar{U}_{y_{j,k}}^{m}}{R\cos(\phi_k + \Delta\phi/2)}\right)\bar{U}_{y_{j,k}}^{m}\sin(\phi_k + \Delta\phi/2)$$
$$- \frac{\Delta t}{R\Delta\lambda\cos(\phi_k + \Delta\phi/2)}\bar{U}_{y_p}^{m}(V_{j,k}^{m} - V_{j-1,k}^{m}) - \frac{\Delta t}{R\Delta\lambda\cos(\phi_k + \Delta\phi/2)}\bar{U}_{y_n}^{m}(V_{j+1,k}^{m} - V_{j,k}^{m})$$
$$- \frac{\Delta t}{R\Delta\phi}V_p^{m}(V_{j,k}^{m} - V_{j,k-1}^{m}) - \frac{\Delta t}{R\Delta\phi}V_n^{m}(V_{j,k+1}^{m} - V_{j,k}^{m}) - n^2 g\frac{\Delta t V_{j,k}^{m}\sqrt{(\bar{U}_{y_{j,k}}^{m})^2 + (V_{j,k}^{m})^2}}{(D_{j,k}^{m} + D_{j,k+1}^{m})^{\frac{4}{3}}} \tag{17}$$

where the subscripts p and n indicate upwind and downwind approximations of the advective speeds and the over bar denotes average quantities.

The momentum-conserved advection scheme of Stelling and Duinmeijer [21] approximates breaking waves as bores or hydraulic jumps and conserves flow volume across discontinuities. Based on their formulation, Yamazaki *et al.* [17] provides the advective speeds in the momentum equations as

$$U_p^{m} = \begin{cases} \dfrac{\hat{U}_{p_{j,k}}^{m} + |\hat{U}_{p_{j,k}}^{m}|}{2} & \text{if } U_{j,k}^{m} \neq 0, \\ 0 & \text{if } U_{j,k}^{m} = 0, \end{cases} \qquad U_n^{m} = \begin{cases} \dfrac{\hat{U}_{n_{j,k}}^{m} - |\hat{U}_{n_{j,k}}^{m}|}{2} & \text{if } U_{j,k}^{m} \neq 0 \\ 0 & \text{if } U_{j,k}^{m} = 0 \end{cases} \tag{18a}$$

$$V_p^{m} = \begin{cases} \dfrac{\hat{V}_{p_{j,k}}^{m} + |\hat{V}_{p_{j,k}}^{m}|}{2} & \text{if } V_{j,k}^{m} \neq 0, \\ 0 & \text{if } V_{j,k}^{m} = 0, \end{cases} \qquad V_n^{m} = \begin{cases} \dfrac{\hat{V}_{n_{j,k}}^{m} - |\hat{V}_{n_{j,k}}^{m}|}{2} & \text{if } V_{j,k}^{m} \neq 0 \\ 0 & \text{if } V_{j,k}^{m} = 0 \end{cases} \tag{18b}$$

where

$$\hat{U}_{p_{j,k}}^{m} = \frac{2FLU_{pj,k}^{m}}{D_{j-1,k}^{m} + D_{j,k}^{m}}, \quad \hat{U}_{n_{j,k}}^{m} = \frac{2FLU_{nj,k}^{m}}{D_{j-1,k}^{m} + D_{j,k}^{m}}, \tag{19a}$$

$$\hat{V}_{p_{j,k}}^{m} = \frac{2FLV_{pj,k}^{m}}{D_{j,k}^{m} + D_{j,k+1}^{m}}, \quad \hat{V}_{n_{j,k}}^{m} = \frac{2FLV_{nj,k}^{m}}{D_{j,k}^{m} + D_{j,k+1}^{m}} \tag{19b}$$

The upwind scheme of Mader [27] determines the flux terms in (19) through extrapolation of the surface elevation instead of the flow depth for improved stability. The flux for a positive flow in the λ direction ($U_{j,k}^{m} > 0$) is given by

$$FLU_{pj,k}^{m} = \begin{cases} \dfrac{U_{j-1,k}^{m} + U_{j,k}^{m}}{2}\left(h_{j-1,k} - \eta_{j-1,k}^{m} + \dfrac{\zeta_{j-2,k}^{m} + \zeta_{j-1,k}^{m}}{2}\right) & \text{if } U_{j-1,k}^{m} > 0 \\ \dfrac{U_{j-1,k}^{m} + U_{j,k}^{m}}{2}(h_{j-1,k} - \eta_{j-1,k}^{m} + \zeta_{j-1,k}^{m}) & \text{if } U_{j-1,k}^{m} < 0 \text{ and } |U_{j,k}^{m}| \geqslant |U_{j-1,k}^{m}| \\ U_{j,k}^{m}\dfrac{D_{j-1,k}^{m} + D_{j,k}^{m}}{2} & \text{if } U_{j-1,k}^{m} < 0 \text{ and } |U_{j,k}^{m}| < |U_{j-1,k}^{m}| \end{cases} \tag{20a}$$

and the flux for a negative flow ($U_{j,k}^{m} < 0$) is

$$FLU_{nj,k}^{m} = \begin{cases} \dfrac{U_{j,k}^{m} + U_{j+1,k}^{m}}{2}\left(h_{j,k} - \eta_{j,k}^{m} + \dfrac{\zeta_{j,k}^{m} + \zeta_{j+1,k}^{m}}{2}\right) & \text{if } U_{j+1,k}^{m} < 0 \\ \dfrac{U_{j,k}^{m} + U_{j+1,k}^{m}}{2}(h_{j,k} - \eta_{j,k}^{m} + \zeta_{j,k}^{m}) & \text{if } U_{j+1,k}^{m} > 0 \text{ and } |U_{j,k}^{m}| \geqslant |U_{j+1,k}^{m}| \\ U_{j,k}^{m}\dfrac{D_{j-1,k}^{m} + D_{j,k}^{m}}{2} & \text{if } U_{j+1,k}^{m} > 0 \text{ and } |U_{j,k}^{m}| < |U_{j+1,k}^{m}| \end{cases} \tag{20b}$$

DOI: 10.1002/fld

Based on the same approach, the flux for a positive flow in the ϕ direction ($V^m_{j,k}>0$) is given by

$$FLV^m_{pj,k}=\begin{cases}\dfrac{V^m_{j,k-1}+V^m_{j,k}}{2}\left(h_{j,k}-\eta^m_{j,k}+\dfrac{\zeta^m_{j,k-1}+\zeta^m_{j,k}}{2}\right) & \text{if } V^m_{j,k-1}>0\\ \dfrac{V^m_{j,k-1}+V^m_{j,k}}{2}(h_{j,k}-\eta^m_{j,k}+\zeta^m_{j,k}) & \text{if } V^m_{j,k-1}<0 \text{ and } |V^m_{j,k}|\geqslant|V^m_{j,k-1}|\\ V^m_{j,k}\dfrac{D^m_{j,k}+D^m_{j,k+1}}{2} & \text{if } V^m_{j,k-1}<0 \text{ and } |V^m_{j,k}|<|V^m_{j,k-1}|\end{cases} \tag{20c}$$

and the flux for a negative flow ($V^m_{j,k}<0$) is

$$FLV^m_{nj,k}=\begin{cases}\dfrac{V^m_{j,k}+V^m_{j,k+1}}{2}\left(h_{j,k+1}-\eta^m_{j,k+1}+\dfrac{\zeta^m_{j,k+1}+\zeta^m_{j,k+2}}{2}\right) & \text{if } V^m_{j,k+1}<0\\ \dfrac{V^m_{j,k}+V^m_{j,k+1}}{2}(h_{j,k+1}-\eta^m_{j,k+1}+\zeta^m_{j,k+1}) & \text{if } V^m_{j,k+1}>0 \text{ and } |V^m_{j,k}|\geqslant|V^m_{j,k+1}|\\ V^m_{j,k}\dfrac{D^m_{j,k}+D^m_{j,k+1}}{2} & \text{if } V^m_{j,k+1}>0 \text{ and } |V^m_{j,k}|<|V^m_{j,k+1}|\end{cases} \tag{20d}$$

The advective speeds $\bar{U}_{yp}$ and $\bar{U}_{yn}$ in the ϕ-momentum equation (17) can be obtained from (18) to (20) by replacing $U^m_{j,k}$, $\zeta^m_{j,k}$, $\eta^m_{j,k}$, and $h_{j,k}$ with average values defined as

$$\bar{U}^m_{y_{j,k}}=\tfrac{1}{4}(U^m_{j,k}+U^m_{j+1,k}+U^m_{j+1,k+1}+U^m_{j,k+1}) \tag{21a}$$

$$\bar{\zeta}^m_{y_{j,k}}=\tfrac{1}{4}(\zeta^m_{j,k}+\zeta^m_{j+1,k}+\zeta^m_{j+1,k+1}+\zeta^m_{j,k+1}) \tag{21b}$$

$$\bar{\eta}^m_{y_{j,k}}=\tfrac{1}{4}(\eta^m_{j,k}+\eta^m_{j+1,k}+\eta^m_{j+1,k+1}+\eta^m_{j,k+1}) \tag{21c}$$

$$\bar{h}_{y_{j,k}}=\tfrac{1}{4}(h_{j,k}+h_{j+1,k}+h_{j+1,k+1}+h_{j,k+1}) \tag{21d}$$

Similarly, $\bar{V}_{xp}$ and $\bar{V}_{xn}$ in the λ-momentum equation (16) can be obtained from (18) to (20) by replacing $V^m_{j,k}$, $\zeta^m_{j,k}$, $\eta^m_{j,k}$, and $h_{j,k}$ with

$$\bar{V}^m_{x_{j,k}}=\tfrac{1}{4}(V^m_{j,k}+V^m_{j-1,k}+V^m_{j-1,k-1}+V^m_{j,k-1}) \tag{22a}$$

$$\bar{\zeta}^m_{x_{j,k}}=\tfrac{1}{4}(\zeta^m_{j,k}+\zeta^m_{j-1,k}+\zeta^m_{j-1,k-1}+\zeta^m_{j,k-1}) \tag{22b}$$

$$\bar{\eta}^m_{x_{j,k}}=\tfrac{1}{4}(\eta^m_{j,k}+\eta^m_{j-1,k}+\eta^m_{j-1,k-1}+\eta^m_{j,k-1}) \tag{22c}$$

$$\bar{h}_{x_{j,k}}=\tfrac{1}{4}(h_{j,k}+h_{j-1,k}+h_{j-1,k-1}+h_{j,k-1}) \tag{22d}$$

This completes the explicit numerical scheme for the nonlinear shallow-water equations in describing hydrostatic flows.

The numerical scheme for the non-hydrostatic solution is implicit. Integration of the non-hydrostatic terms in the horizontal momentum equations updates the horizontal velocity from (16) and (17) to

$$U^{m+1}_{j,k}=\tilde{U}^{m+1}_{j,k}-\frac{\Delta t}{R\Delta\lambda\cos\phi_k}A_{j,k}\frac{(q^{m+1}_{j,k}+q^{m+1}_{j-1,k})}{2}-\frac{\Delta t}{R\Delta\lambda\cos\phi_k}\frac{(q^{m+1}_{j,k}-q^{m+1}_{j-1,k})}{2} \tag{23}$$

$$V^{m+1}_{j,k}=\tilde{V}^{m+1}_{j,k}-\frac{\Delta t}{R\Delta\phi}B_{j,k}\frac{(q^{m+1}_{j,k+1}+q^{m+1}_{j,k})}{2}-\frac{\Delta t}{R\Delta\phi}\frac{(q^{m+1}_{j,k+1}-q^{m+1}_{j,k})}{2} \tag{24}$$

DOI: 10.1002/fld

where

$$A_{j,k}=\frac{(\zeta^m_{j,k}-h_{j,k}+\eta^m_{j,k})-(\zeta^m_{j-1,k}-h_{j-1,k}+\eta^m_{j-1,k})}{(D^m_{j,k}+D^m_{j-1,k})} \tag{25a}$$

$$B_{j,k}=\frac{(\zeta^m_{j,k+1}-h_{j,k+1}+\eta^m_{j,k+1})-(\zeta^m_{j,k}-h_{j,k}+\eta^m_{j,k})}{(D^m_{j,k}+D^m_{j,k+1})} \tag{25b}$$

Discretization of the vertical momentum equation (11) gives the vertical velocity at the free surface as

$$w^{m+1}_{s_{j,k}}=w^m_{s_{j,k}}-(w^{m+1}_{b_{j,k}}-w^m_{b_{j,k}})+\frac{2\Delta t}{D^m_{j,k}}q^{m+1}_{j,k} \tag{26}$$

The vertical velocity on the seafloor is evaluated from the boundary condition (7) as

$$w^{m+1}_{b_{j,k}}=\frac{\eta^{m+1}_{j,k}-\eta^m_{j,k}}{\Delta t}-\bar{U}^m_{z_p}\frac{(h_{j,k}-\eta^m_{j,k})-(h_{j-1,k}-\eta^m_{j-1,k})}{R\Delta\lambda\cos\phi_k}-\bar{U}^m_{z_n}\frac{(h_{j+1,k}-\eta^m_{j+1,k})-(h_{j,k}-\eta^m_{j,k})}{R\Delta\lambda\cos\phi_k}$$
$$-\bar{V}^m_{z_p}\frac{(h_{j,k}-\eta^m_{j,k})-(h_{j,k-1}-\eta^m_{j,k-1})}{R\Delta\phi}-\bar{V}^m_{z_n}\frac{(h_{j,k+1}-\eta^m_{j,k+1})-(h_{j,k}-\eta^m_{j,k})}{R\Delta\phi} \tag{27}$$

in which

$$\bar{U}^m_{z_p}=\frac{\bar{U}^m_{z_{j,k}}+|\bar{U}^m_{z_{j,k}}|}{2},\quad \bar{U}^m_{z_n}=\frac{\bar{U}^m_{z_{j,k}}-|\bar{U}^m_{z_{j,k}}|}{2};\quad \bar{V}^m_{z_p}=\frac{\bar{V}^m_{z_{j,k}}+|\bar{V}^m_{z_{j,k}}|}{2},\quad \bar{V}^m_{z_n}=\frac{\bar{V}^m_{z_{j,k}}-|\bar{V}^m_{z_{j,k}}|}{2} \tag{28}$$

where

$$\bar{U}^m_{z_{j,k}}=\frac{U^m_{j,k}+U^m_{j+1,k}}{2},\quad \bar{V}^m_{z_{j,k}}=\frac{V^m_{j,k}+V^m_{j,k-1}}{2} \tag{29}$$

The horizontal velocity components and the vertical velocity at the free surface are now expressed in terms of the non-hydrostatic pressure.

The non-hydrostatic pressure $q^{m+1}_{j,k}$ is calculated implicitly using the continuity equation (4) discretized in the form

$$\frac{U^{m+1}_{j+1,k}-U^{m+1}_{j,k}}{R\Delta\lambda\cos\phi_k}+\frac{V^{m+1}_{j,k}\cos(\phi_k+\Delta\phi/2)-V^{m+1}_{j,k-1}\cos(\phi_{k-1}+\Delta\phi/2)}{R\Delta\phi\cos\phi_k}+\frac{w^{m+1}_{s_{j,k}}-w^{m+1}_{b_{j,k}}}{D^m_{j,k}}=0 \tag{30}$$

Substitution of (23), (24), and (26) into the continuity equation (30) gives a linear system of Poisson-type equations at each cell

$$PL_{j,k}q^{m+1}_{j-1,k}+PR_{j,k}q^{m+1}_{j+1,k}+PB_{j,k}q^{m+1}_{j,k-1}+PT_{j,k}q^{m+1}_{j,k+1}+PC_{j,k}q^{m+1}_{j,k}=Q_{j,k} \tag{31}$$

where the coefficients are

$$PL_{j,k}=\frac{1}{\cos\phi^2_k}\frac{\Delta t}{2(R\Delta\lambda)^2}(-1+A_{j,k}) \tag{32a}$$

$$PR_{j,k}=\frac{1}{\cos\phi^2_k}\frac{\Delta t}{2(R\Delta\lambda)^2}(-1-A_{j+1,k}) \tag{32b}$$

$$PB_{j,k}=\frac{\cos(\phi_{k-1}+\Delta\phi/2)}{\cos\phi_k}\frac{\Delta t}{2(R\Delta\phi)^2}(-1+B_{j,k-1}) \tag{32c}$$

$$PT_{j,k}=\frac{\cos(\phi_k+\Delta\phi/2)}{\cos\phi_k}\frac{\Delta t}{2(R\Delta\phi)^2}(-1-B_{j,k}) \tag{32d}$$

DOI: 10.1002/fld

$$PC_{j,k}=\frac{1}{\cos\phi_k^2}\frac{\Delta t}{2(R\Delta\lambda)^2}[(1+A_{j,k})+(1-A_{j+1,k})]$$
$$+\frac{1}{\cos\phi_k}\frac{\Delta t}{2(R\Delta\phi)^2}[(1+B_{j,k-1})\cos(\phi_{k-1}+\Delta\phi/2)+(1-B_{j,k})\cos(\phi_k+\Delta\phi/2)]$$
$$+\frac{2\Delta t}{(D_{j,k}^m)^2} \tag{32e}$$

and the forcing term is

$$Q_{j,k}=-\frac{\tilde{U}_{j+1,k}^{m+1}-\tilde{U}_{j,k}^{m+1}}{R\Delta\lambda\cos\phi_k}-\frac{\tilde{V}_{j,k}^{m+1}\cos(\phi_k+\Delta\phi/2)-\tilde{V}_{j,k-1}^{m+1}\cos(\phi_{k-1}+\Delta\phi/2)}{R\Delta\phi\cos\phi_k}$$
$$-\frac{w_{s_{j,k}}^m+w_{b_{j,k}}^m-2w_{b_{j,k}}^{m+1}}{D_{j,k}^m} \tag{33}$$

The terms $A_{j,k}$, $B_{j,k}$, and $Q_{j,k}$ describe the seafloor, free-surface, and velocity gradients in the generation and modification of dispersive waves. Assembly of (31) at all grid cells gives rise to a matrix equation in the form of

$$[P]\{q\}=\{Q\} \tag{34}$$

which provides the non-hydrostatic pressure at each time step. The matrix equation (34), in which $[P]$ is nonsymmetric, can be solved by the strongly implicit procedure (SIP) of Stone [31]. At each time step, the computation starts with the calculation of the hydrostatic solution of the horizontal velocity using (16) and (17). The non-hydrostatic pressure is then calculated using (34) and the horizontal velocity is updated with (23) and (24) to account for the non-hydrostatic effects. The computation for the non-hydrostatic solution is complete with the calculation of the free surface elevation as well as the free surface and the bottom vertical velocities from (13), (26), and (27), respectively.

The governing equations in the spherical coordinate system (λ, ϕ) can be transformed into the Cartesian system (x, y) for modeling of a coastal region or a laboratory experiment. Effects of the earth's curvature is insignificant and the grid spacing in the x and y directions becomes

$$\Delta x=R\Delta\lambda\cos\phi_k,\quad \Delta y=R\Delta\phi \tag{35}$$

The Coriolis terms in the horizontal momentum equations (16) and (17) vanish

$$\left(2\Omega+\frac{U_{j,k}^m}{R\cos\phi_k}\right)\bar{V}_{x_{j,k}}^m\sin\phi_k=0 \tag{36a}$$

$$\left(2\Omega+\frac{\bar{U}_{y_{j,k}}^m}{R\cos(\phi_k+\Delta\phi/2)}\right)\bar{U}_{y_{j,k}}^m\sin(\phi_k+\Delta\phi/2)=0 \tag{36b}$$

Since the grid cells do not taper off in the north–south direction, we can simply set $\phi=0$. These modifications will recover the numerical formulation in the Cartesian coordinate system as derived by Yamazaki *et al.* [17].

3. NUMERICAL IMPLEMENTATION

The depth-integrated, non-hydrostatic model provides a general framework to describe dispersion and breaking of ocean waves over variable bottom. This section discusses its implementation with a two-way grid-nesting scheme and a bathymetry-smoothing strategy for modeling of the

DOI: 10.1002/fld

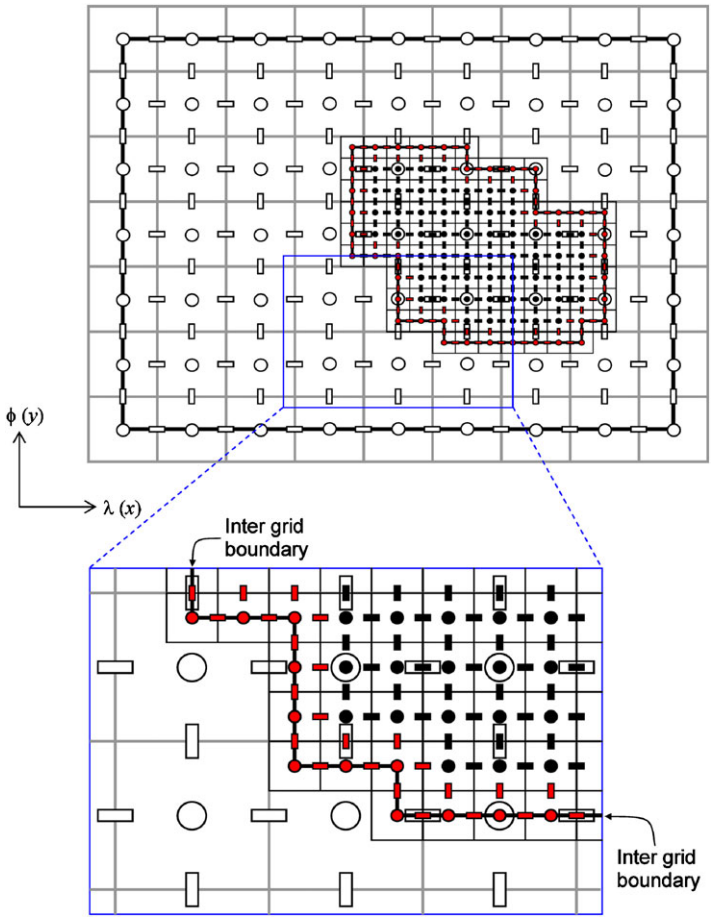

Figure 3. Schematic of a two-level nested grid system.

tsunami evolution processes from generation to run-up. The grid-nesting scheme utilizes a flexible indexing system that enables adaptation of inter-grid boundaries to topographic features for optimal resolution and computational efficiency. The smoothing scheme generalizes the stability criterion of Horrillo *et al.* [11] to remove small-scale bathymetric features in relation to the water depth that cannot be resolved by non-hydrostatic or Boussinesq-type models.

3.1. Grid-nesting scheme

Most grid-nesting schemes for tsunami models use a system of rectangular grids with the fluxes as input to a fine inner grid and the surface elevation as output to the outer grid [5, 6, 8]. A non-hydrostatic model needs to input the horizontal velocity, surface elevation as well as the non-hydrostatic pressure to ensure propagation of breaking and dispersion waves across inter-grid boundaries. Figure 3 illustrates the grid setup and data transfer protocol. The outer and inner grids align at the cell centers, where they share the same water depth. The scheme allows the flexibility to define inter-grid boundaries at any location within the inner grid network analogous to the quadtree and adaptive grids [32–34]. The surface elevation and non-hydrostatic pressure are input at the cell centers as indicated by the red dots in the figure. While the tangential component of the velocity is applied along the inter-grid boundary, the normal component is applied on the inboard side of the boundary cells as indicated by the red dash. Existing grid-nesting schemes, which only input the normal velocity, cannot handle propagation of discontinuities and Coriolis effects across inter-grid boundaries.

DOI: 10.1002/fld

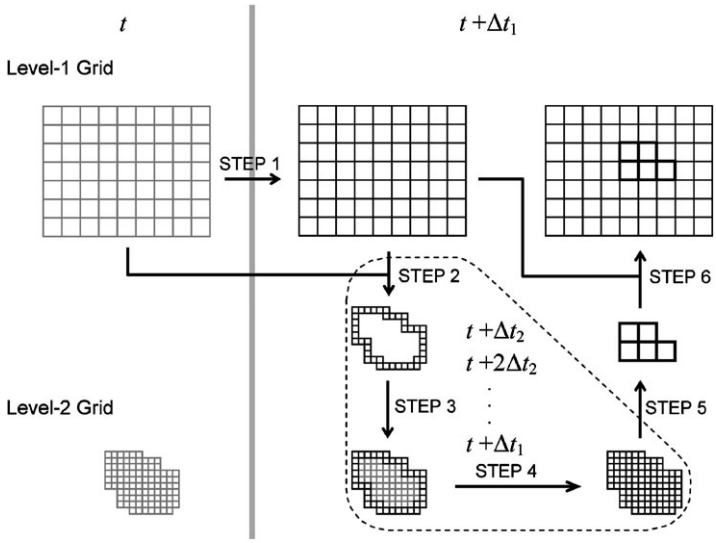

Figure 4. Schematic of two-way grid-nesting and time-integration schemes.

Figure 4 shows a schematic of the solution procedure with the two-way grid-nesting scheme. The time step Δt_1 of the outer grid must be divisible by the inner-grid time step Δt_2. The calculation begins at time t with the complete solutions at both the outer and inner grids. The time-integration procedure provides the solution over the outer grid at $(t+\Delta t_1)$. Linear interpolation of the horizontal velocity, surface elevation, and non-hydrostatic pressure in time and space provides the input boundary conditions to the inner grid. The time-integration procedure then computes the inner grid solution at Δt_2 increments until $(t+\Delta t_1)$. The hydrostatic solution is computed explicitly from the input surface elevation and horizontal velocity. The non-hydrostatic solution is implicit and requires reorganization of the matrix equation (34) for the input non-hydrostatic pressure from the outer grid. The simple dispersive terms with first-order derivatives allow implementation of the Dirichlet condition to enable wave dispersion across inter-grid boundaries. After the computation in the inner grid reaches $(t+\Delta t_1)$, the surface elevation at the outer grid is then updated with the average value from the overlapping inner grid cells to complete the procedure. This feedback mechanism is similar to the grid-nesting scheme of Goto *et al.* [6] for hydrostatic models.

The implementation of the Dirichlet boundary condition requires modification of the Poisson-type equation (31) at the cells along the inter-grid boundary. For example, if the non-hydrostatic pressure is input from the left (west), the corresponding pressure term becomes part of the forcing on the right-hand side as

$$PR_{j,k}q^{m+1}_{j+1,k}+PB_{j,k}q^{m+1}_{j,k-1}+PT_{j,k}q^{m+1}_{j,k+1}+PC_{j,k}q^{m+1}_{j,k}=Q_{j,k}-PL_{j,k}q^{m+1}_{j-1,k} \tag{37}$$

Similarly, if the non-hydrostatic pressure is defined at the bottom (south), (31) becomes

$$PL_{j,k}q^{m+1}_{j-1,k}+PR_{j,k}q^{m+1}_{j+1,k}+PT_{j,k}q^{m+1}_{j,k+1}+PC_{j,k}q^{m+1}_{j,k}=Q_{j,k}-PB_{j,k}q^{m+1}_{j,k-1} \tag{38}$$

When the non-hydrostatic pressure is input from the left (west) and bottom (south), the Dirichlet boundary condition gives rise to

$$PR_{j,k}q^{m+1}_{j+1,k}+PT_{j,k}q^{m+1}_{j,k+1}+PC_{j,k}q^{m+1}_{j,k}=Q_{j,k}-PL_{j,k}q^{m+1}_{j-1,k}-PB_{j,k}q^{m+1}_{j,k-1} \tag{39}$$

Similar equations can be defined for cells with input from the right (east) and top (north). This approach allows implementation of the Dirichlet boundary condition along irregular inter-grid boundaries to construct the matrix equation (34), from which the non-hydrostatic pressure in the inner grid can be determined.

DOI: 10.1002/fld

3.2. Bathymetry smoothing schemes

The present depth-integrated, non-hydrostatic model is generally stable, but the implicit solver for the non-hydrostatic pressure does not always converge when the bathymetry includes small features relative to the water depth. Horrillo *et al.* [11] discussed similar convergence issues with the dispersion terms in the classical Boussinesq equations and derived the stability criterion $\Delta x > 1.5\,\mathrm{h}$ from their numerical formulation. Løvholt and Pederson [26] also showed that Boussinesq-type models are prone to instability over localized, steep bottom gradients at high-resolution computations. They pointed out that the instability is probably due to the dispersion terms. If the instability is inherent in the theoretical formulation, it is difficult to resolve the issue through refinements of numerical schemes. Smoothing of the bathymetry appears to be a typical solution to stability problems associated with Boussinesq-type models, although Plant *et al.* [35] pointed out such numerical treatments might alter the wave field in the near-shore region.

Preliminary numerical tests have shown that the present implicit solver could achieve convergence for flow over irregular bathymetry with properly selected grid sizes in relation to the water depth. Such an approach, however, is not feasible as a treatment for local bathymetric features with steep gradients in the open ocean. We utilize a depth-dependent Gaussian function to resolve stability issues arising from local bathymetric features in deep water and to minimize unnecessary alternations of the bathymetry in near-shore waters. The smoothing scheme has a variable search diameter in terms of the water depth $h_{j,k}$ as

$$\Delta D_{j,k} = \alpha h_{j,k} \tag{40}$$

where $\alpha > 1.5$ in accordance to the stability criterion of Horrillo *et al.* [11]. In the implementation, the smoothed water depth is given by

$$h_{j,k} = \sum_{\tilde{j}=j-n/2}^{j+n/2} \sum_{\tilde{k}=k-n/2}^{k+n/2} w_{\tilde{j},\tilde{k}} h_{o_{\tilde{j},\tilde{k}}} \tag{41}$$

where $w_{\tilde{j},\tilde{k}}$ is a weight function, $h_{o_{\tilde{j},\tilde{k}}}$ is the original bathymetry, and n is the number of grid cells within the search diameter $\Delta D_{j,k}$. The weight function is expressed as

$$w_{\tilde{j},\tilde{k}} = G_{\tilde{j},\tilde{k}} \left(\sum_{\hat{j}=j-n/2}^{j+n/2} \sum_{\hat{k}=k-n/2}^{k+n/2} G_{\hat{j},\hat{k}} \right)^{-1} \tag{42}$$

in which the Gaussian function is defined as

$$G_{\tilde{j},\tilde{k}} = \frac{2}{\pi \Delta D_{j,k}^2} \exp\left(-\frac{2 r_{\tilde{j},\tilde{k}}^2}{\Delta D_{j,k}^2} \right) \tag{43}$$

where $r_{\tilde{j},\tilde{k}}$ is the distance between the points $(\tilde{j},\tilde{k})$ and (j,k). This scheme smoothes features with characteristic dimensions less than αh to accommodate smaller computational cells to resolve dispersive waves in the open ocean.

The use of nested grids requires additional attention with complex bathymetry and topography. The grid resolution changes abruptly from one level to the next. The resolution of the relief data needs to transition gradually across inter-grid boundaries to facilitate exchange of compatible flow parameters. We interpolate the outer grid bathymetry at the inner grid cells along the inter-grid boundary and gradually transition the resolution of the bathymetry to that of the inner grid over two outer grid cells. The interpolation scheme assures that the solutions in the inner and outer grids are computed from the same bathymetry along the inter-grid boundary. This procedure becomes imperative in coastal waters when the inter-grid boundary intersects the coastline and interpolation of flow parameters occurs across the wet-dry boundary.

DOI: 10.1002/fld

4. VERIFICATION OF GRID-NESTING SCHEME

The proposed grid-nesting scheme is unique among existing approaches and needs a systematic evaluation prior to its implementation for modeling of real-field tsunamis. We first verify the grid-nesting scheme through numerical experiments of solitary wave propagation in a channel and N-wave run-up in a laboratory basin. The coordinate transformation (37) and (38) reduces the computational grids to the Cartesian system because of the small computational domains, but the grid-nesting scheme remains the same.

4.1. Solitary wave propagation

The propagation of a solitary wave in uniform water depth is a standard test case for dispersive wave models. This represents a delicate balance between nonlinear steepening and dispersive spreading to provide a critical test for the grid-nesting scheme. The model must accurately transfer the flow kinematics and non-hydrostatic pressure and balance the nonlinear and dispersive effects across inter-grid boundaries to maintain the solitary waveform. We consider a 45-m long, 25-m wide, and 0.5-m deep channel with two levels of nested grids. The initial conditions correspond to a 0.05-m high solitary wave at $x = 7.5$ m. Radiation conditions at both ends of the channel minimize reflection and a Manning's roughness coefficient $n = 0$ corresponds to an inviscid flow.

Figure 5 shows a sequence of the computed waveforms in their original resolution as the solitary wave propagates through the finer inner grid. The numerical experiment uses 20 cm resolution for the level-1 outer grid and 4 cm for the level-2 inner grid. The configuration of the level-2 grid allows testing of solitary wave propagation at different directions with respect to the inter-grid boundary. The solitary wave enters the level-2 grid around $t = 2.5$ s and leaves at 15.0 s. Although the inter-grid boundary is oblique to the wave direction, the solitary wave passes through the level-2 grid smoothly with invisible surface disturbance and leaves no residual oscillations near the inter-grid boundary, thereby verifying the capability of the grid-nesting scheme for dispersive wave propagation.

4.2. N-wave transformation and run-up

Matsuyama and Tanaka [25] conducted a laboratory study at the Central Research Institute for Electric Power Industry (CRIEPI) to investigate the nearshore wave dynamics of the 1993 Hokkaido Nansei-Oki Tsunami. Eyewitness reported initial withdraw of the water followed by a large tsunami wave at the coast causing 31.7 m of run-up near Monai Valley, Japan. Such observations fit the description of the leading depression N-wave, which is often used in laboratory studies of tsunami impact close to the source. The CRIEPI wave flume is 205 m long, 3.4 m wide, and 6 m high with a hydraulic, piston-type wavemaker capable of generating N-waves. The 1:400-scale coastal relief model around Monai Valley was constructed of painted plywood and installed approximately 140 m from the wavemaker. The initial N-wave, which was relatively long with a very gentle profile, dispersed into a series of short-period waves over the coastal relief model in the experiment. The measured water-level data and run-up from the experiment allow validation of the present grid-nesting scheme in describing generation of dispersive waves across inter-grid boundaries.

Figure 6(a) shows the setup of the numerical experiment over the 5.475-m long and 3.4-m wide relief model. The level-1 grid covers the entire relief model at 2.5 cm resolution (10 m full scale) and the level-2 grid at 1.25 cm resolution (5 m full scale) provides a more detailed description of the wave processes in a nearshore area from Monai Valley to the 0.035-m (14 m full-scale) depth contour. A Manning's coefficient $n = 0.012$ describes the surface roughness of the painted plywood relief model [36]. Figure 6(b) shows the input N-wave profile at the left boundary with 0.135 m (54 m full scale) water depth. The incident waves shoal over a plane slope before refracting and diffracting around a small island on a shallow bank. Figure 7(a) shows very good agreement of the computed surface elevations with the laboratory measurements at three gauges behind the island. The model reproduces the small-amplitude dispersive waves generated by reflection from the coast. The minor phase lag in the dispersive waves is likely due to errors in the small-scale laboratory experiment. We recomputed the results with a uniform grid over the entire domain at the same

DOI: 10.1002/fld

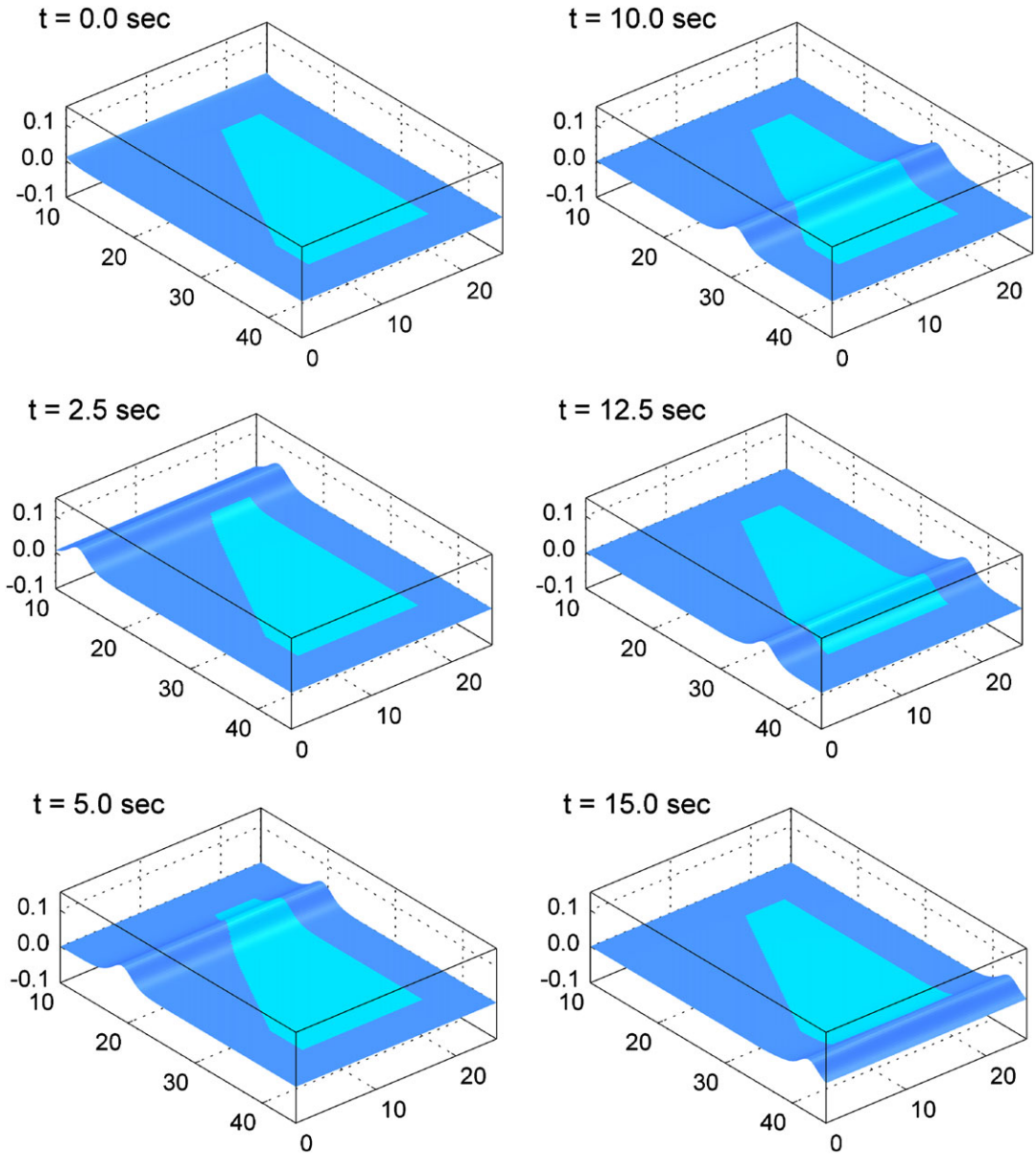

Figure 5. Propagation of solitary wave across two levels of nested grids in a channel of constant depth. Dark blue indicates the level-1 grid and light blue denotes the level-2 grid.

1.25 cm resolution as the level-2 nested grid and obtained almost identical results as shown in Figure 7(b).

Table I lists the run-up measurements along transects at $y = 2.2062$ and 2.32 m as well as the maximum value inside Monai Valley from a series of tests in the laboratory experiment of Matsuyama and Tanaka [25]. Figure 8 shows the computed run-up and inundation from the nested and uniform grids along with the range and mean value of the recorded run-up. The computed results show good agreement with the measured data despite the uncertainty in the laboratory experiment. Both the nested and the uniform grid solutions are almost identical indicating the proposed grid-nesting scheme appropriately transfers information across the inter-grid boundary and provide results of comparable accuracy at a lower computational cost. The minor discrepancies near the inter-grid boundaries are due to transition of the bathymetry from the outer to the inner grid. Comparisons of the surface elevation, run-up, and inundation from the Moani Valley experiment

DOI: 10.1002/fld

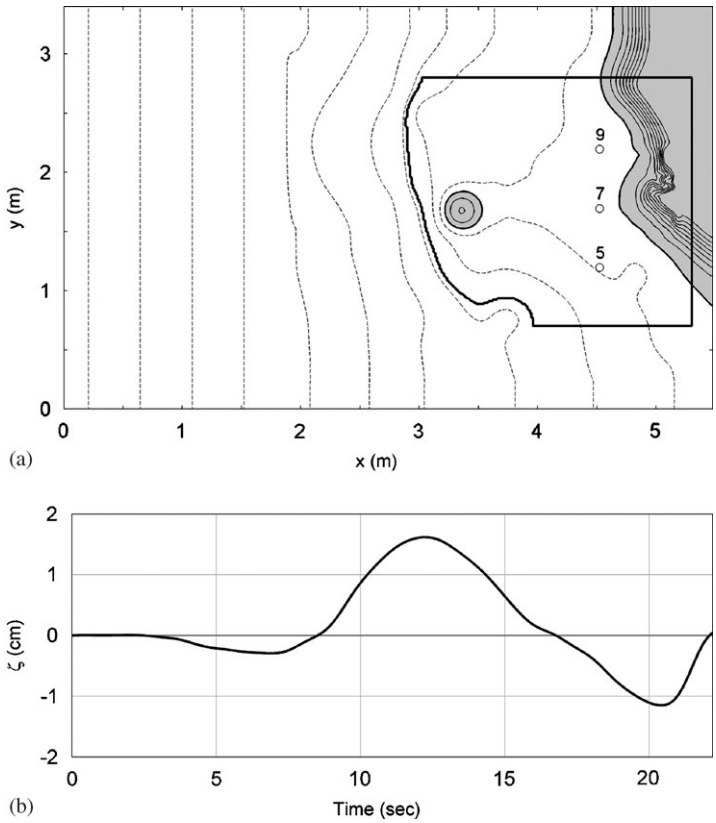

Figure 6. (a) Level-1 and Level-2 computational domains for the Monai Valley Experiment. ○, gauge locations; —— (black), topography contours at 0.0125-m intervals; - - - - (gray), bathymetry contours at 0.0125-m intervals. (b) Input N-wave for the Monai valley experiment.

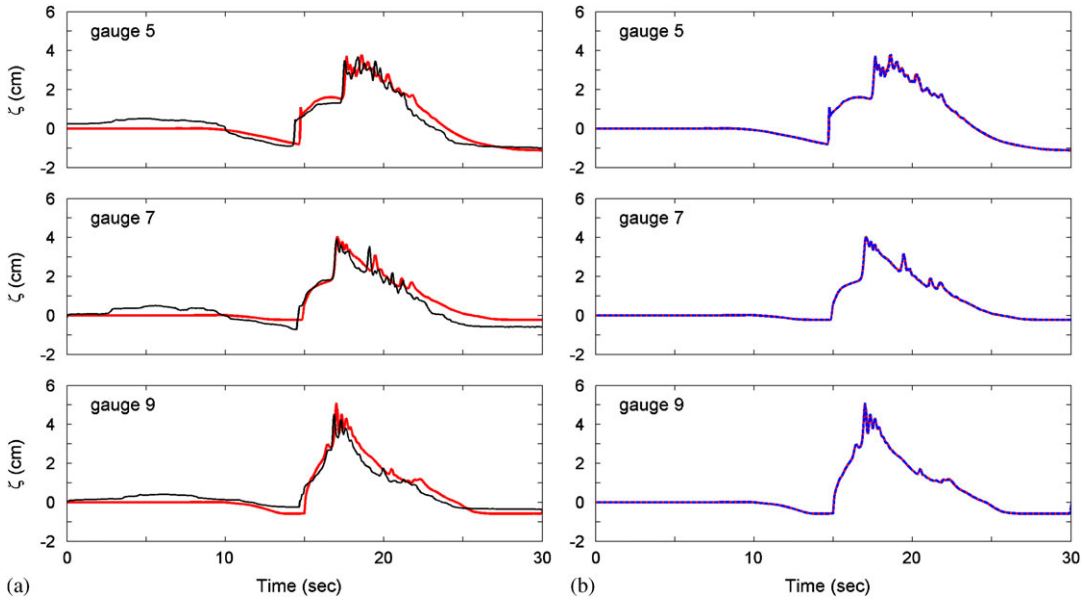

Figure 7. Time series of surface elevation at gauges in Monai Valley experiment: (a) comparison of measurements with nested-grid solution and (b) comparison of nested and uniform grid solutions. —— (black), laboratory data of Matsuyama and Tanaka [25]; —— (red), nested-grid solution; - - - (blue), uniform-grid solution.

DOI: 10.1002/fld

Table I. Recorded run-up for the six trials from Matsuyama and Tanaka [25].

Trial no.	Maximum R_{max} (cm) (Full scale in m)	$y=2.2062$ m R (cm) (Full scale in m)	$y=2.32$ m R (cm) (Full scale in m)
209_105	8.75 (35.0)	5.25 (21.0)	5.25 (21.0)
209_106	9.00 (36.0)	5.75 (23.0)	5.50 (22.0)
209_107	8.00 (32.0)	5.50 (22.0)	5.50 (22.0)
210_101	9.00 (36.0)	6.50 (26.0)	5.75 (23.0)
210_102	10.00 (40.0)	6.75 (27.0)	5.75 (23.0)
210_103	9.00 (36.0)	6.50 (26.0)	5.75 (23.0)
Mean	8.97 (35.8)	6.04 (24.2)	5.58 (22.3)

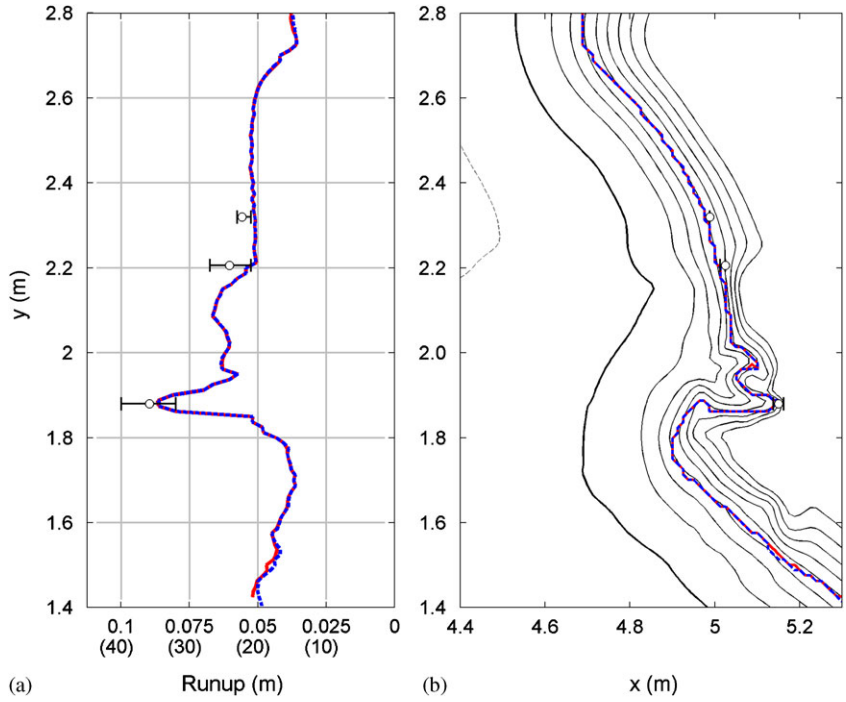

Figure 8. Run-up and inundation in Monai Valley experiment: (a) run-up and (b) inundation. ○, laboratory data of Matsuyama and Tanaka [25]; —— (red), nested-grid solution; - - - (blue), uniform-grid solution; —— (black), topography contours at 0.0125 m intervals; - - - (gray), bathymetry contours at 0.0125 m intervals.

verify the proposed grid-nesting scheme in handling dispersive wave and run-up processes over complex nearshore bathymetry and topography.

5. MODEL VALIDATION AND DISCUSSION

We have incorporated the spherical coordinate system and two-way grid-nesting scheme into the model NEOWAVE (Non-hydrostatic Evolution of Ocean WAVE) of Yamazaki *et al.* [17]. This allows modeling of tsunami evolution processes from generation, propagation to run-up with due consideration to dynamic seafloor deformation, wave dispersion, wave breaking, and bore propagation at appropriate resolution. The 2009 Samoa Tsunami affected regions with steep and irregular offshore bathymetry as well as extended shallow fringing reefs. The well-recorded event provides a critical test case to validate the present grid-nesting scheme and bathymetry smoothing strategy for real-field tsunami modeling.

DOI: 10.1002/fld

5.1. Test case and model setup

The Samoa earthquake occurred near the Tonga trench on 29 September 2009 at 17:48:10 UTC. The US Geological Survey (USGS) determined the epicenter at 15.509°S 172.034°W and estimated the moment magnitude M_w of 8.1. Figure 9 shows the rupture configuration and the locations of the water-level stations in the region. The main energy of the resulting tsunami propagated toward Tonga and American Samoa. The tide gauge in Pago Pago Harbor, Tutuila (American Samoa), and the DART buoys 51425, 51426, and 54401 surrounding the rupture area recorded clear signals of the tsunami. The destructive waves arrived at mid tide and produced a maximum run-up of 17.6 m with detrimental impact on Tutuila. The rugged, volcanic island sits on a shallow shelf of less than 100 m depth covered by mesophotic corals [37]. The insular slope is steep with gradients up to 1:2 on the west side and drops off abruptly to over 3000 m depth in the surrounding ocean. Several field survey teams recorded and documented the tsunami run-up and inundation around Tutuila and provided useful data for model validation [38–40].

We reconstruct the 2009 Samoa Tsunami from its generation at the earthquake source to run-up at Pago Pago Harbor with four levels of nested grids. Figure 9(a) shows the coverage of the level-1 grid, which extends across the south-central Pacific at 1-arcmin (≈1800 m) resolution. An open boundary condition allows radiation of tsunami waves away from the domain. Figure 10 shows the original and the smoothed bathymetry at the next three levels. The level-2 grid covers American Samoa and the surrounding seabed inside the 4000-m depth contour at 7.5 arcsec (≈225 m) resolution to capture wave transformation around the island group. The level-3 grid resolves the insular shelf and slope of Tutuila down to the 1500-m depth contour at 1.5 arcsec (∼45 m) and provides a transition to the level-4 grid, which covers Pago Pago Harbor at 0.3 arcsec (∼9 m) resolution for computation of inundation as well as tide gauge signals. This nested-grid system describes wave dynamics at resolution compatible with the physical process and spatial scale for optimization of computational resources. A Manning's coefficient $n = 0.035$ represents the surface roughness of the coral reefs in the near-shore seabed according to Bretschneider *et al*. [41]. The momentum-conserved advection

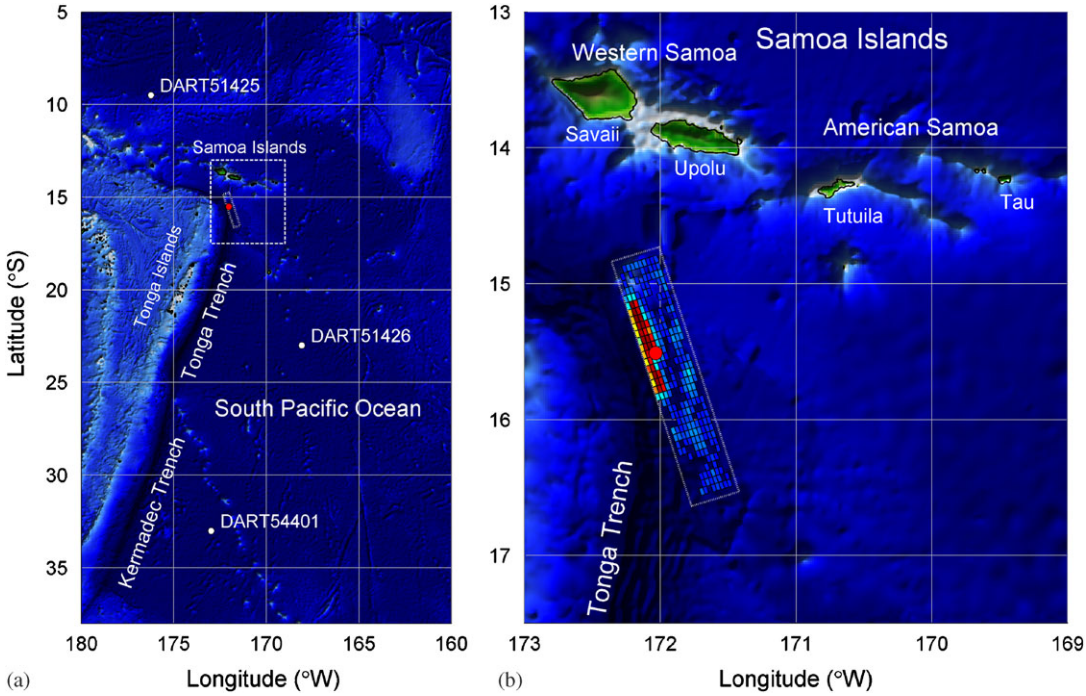

Figure 9. Bathymetry and topography in the model region for the 2009 Samoa Tsunami: (a) level-1 computational domain and (b) close-up view of rupture configuration and Samoa Islands. ....., rupture area; ○ (red), epicenter; ○ (white), water-level stations.

DOI: 10.1002/fld

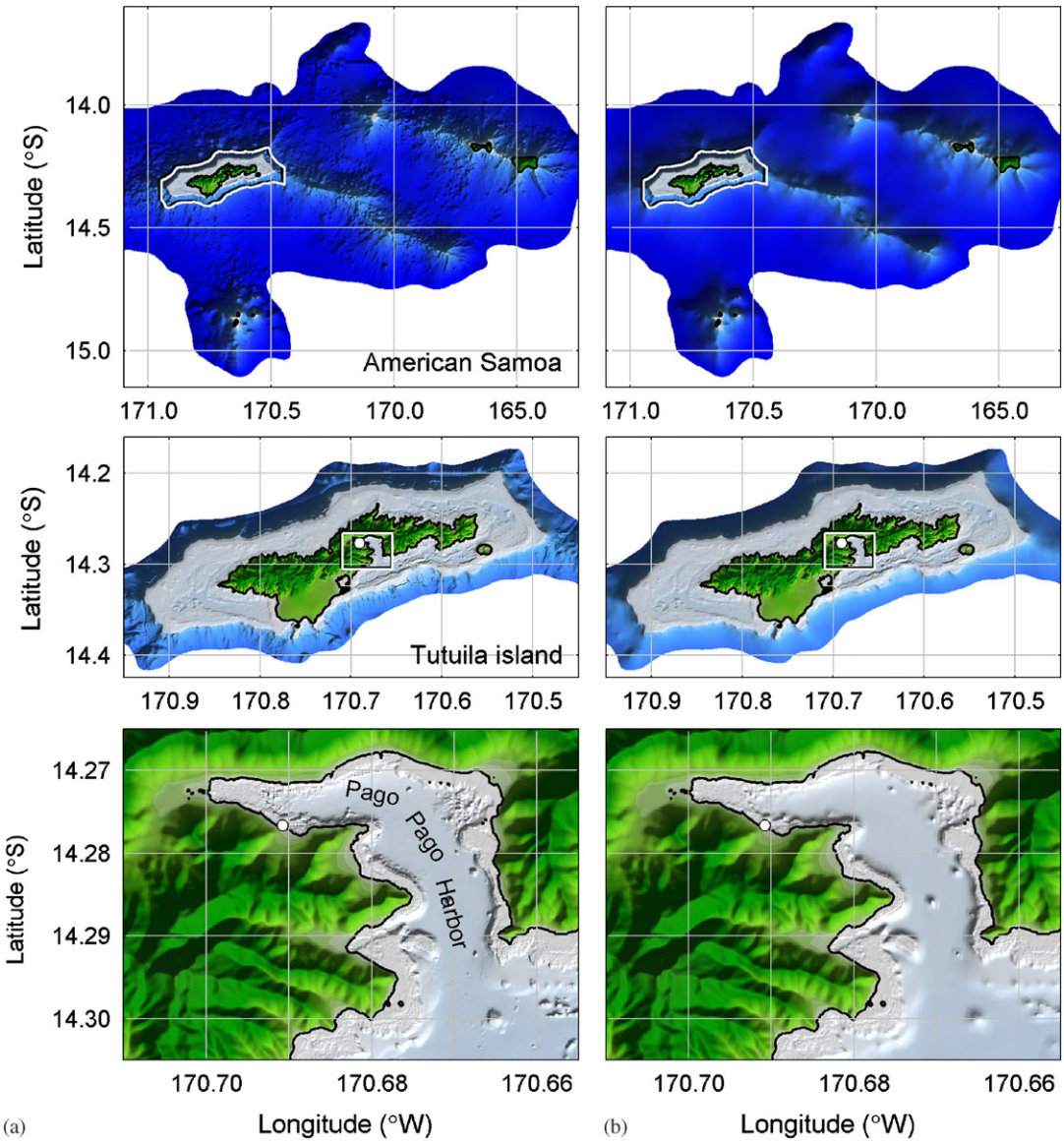

Figure 10. Coverage of level-2, level-3, and level-4 computational domains: (a) original bathymetry and topography and (b) smoothed data with depth-dependent Gaussian function. ○, Pago Pago tide station.

scheme is used at the level-4 grid, where flow discontinuities associated with wave breaking and bore formation would otherwise cause volume loss and numerical dissipation.

The digital elevation model is derived from a blended dataset of multiple sources. The 0.5 arcmin (≈900 m) General Bathymetric Chart of the Oceans (GEBCO) from the British Oceanographic Data Centre (BODC) provides the bathymetry for Pacific Ocean. The Coastal Relief Model from National Geophysical Data Center (NGDC) covers the American Samoa region and Tutuila at 3 and 0.3333 arcsec (∼90 and 10 m) resolution, respectively. Embedded in the NGDC dataset are multibeam and satellite measurements around Tutuila and high-resolution LiDAR (Light Detection and Ranging) survey data at Pago Pago Harbor. We have converted the datasets to reference the WGS 84 datum and the mean sea level (MSL). The Generic Mapping Tools (GMT) interpolates the data to produce the nested computational grids. The original data in Figure 10(a) shows fine details of the seafloor. Smoothing of the bathymetry is sometimes necessary to ensure a converging solution from the non-hydrostatic model. Figure 10(b) shows the processed data with the depth-dependent

DOI: 10.1002/fld

Gaussian function. The proposed scheme removes fine features in deep water that have little effect on tsunami propagation, but retains the general bathymetry and the near-shore details important for propagation and inundation computation, respectively.

5.2. *Tsunami generation*

The use of the vertical velocity to describe dispersive waves also facilitates modeling of tsunami generation through dynamic deformation of the seafloor. USGS analyzed the rupture processes of the 2009 Samoa Earthquake using the finite fault inverse algorithm of Ji *et al.* [24] and estimated the fault parameters, such as depth, orientation, and slip over 420 subfaults of 6 km by 6 km each. The analysis provides the rupture initiation time and rise time for 249 subfaults with seismic moment of over 10^{25} dyne-cm each.

The planar fault model of Okada [42] describes the earth surface deformation in terms of the depth, orientation, and slip of a rectangular fault as shown in Figure 11. The deformation is a linear function of the slip and dimensions of the fault. Superposition of the planar fault solutions from the subfaults gives the vertical displacement of the seafloor as

$$\eta(\lambda, \phi, t) = \sum_{i=1}^{n} \eta_i(\lambda, \phi) f_i(t) \tag{44}$$

in which

$$f_i(t) = \begin{cases} 0 & \text{if } t < t_i \\ \dfrac{t - t_i}{\tau_i} & \text{if } t_i \leqslant t \leqslant (t_i + \tau_i) \\ 1 & \text{if } t > (t_i + \tau_i) \end{cases} \tag{45}$$

where $n = 249$ is the number of subfaults for the 2009 Samoa Earthquake, η_i is the vertical earth surface deformation associated with rupture of subfault i from Okada [42], and t_i and τ_i are the corresponding rupture initiation time and rise time from the USGS finite fault solution. The source time function (45) defines a linear motion of the slip at each subfault to approximate the rupture process in the absence of more detailed information [43].

The USGS finite fault solution shows an average rise time of 3.4 s for the individual subfaults and a rupture duration of 94 s over the entire event. Figure 12 shows the rupture, seafloor deformation, and free surface elevation to illustrate the tsunami generation process. The rupture starts at the epicenter located on the north side of the fault and propagates toward south. Despite the granularity of the finite fault model, the seafloor deformation is rather continuous due to the depth of the fault below the earth surface. The rupture generates a distinct pattern of uplift and subsidence on the

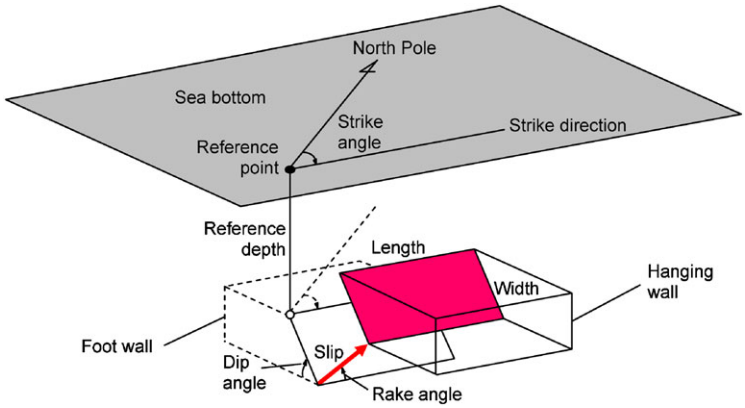

Figure 11. Schematic of planar fault model.

DOI: 10.1002/fld

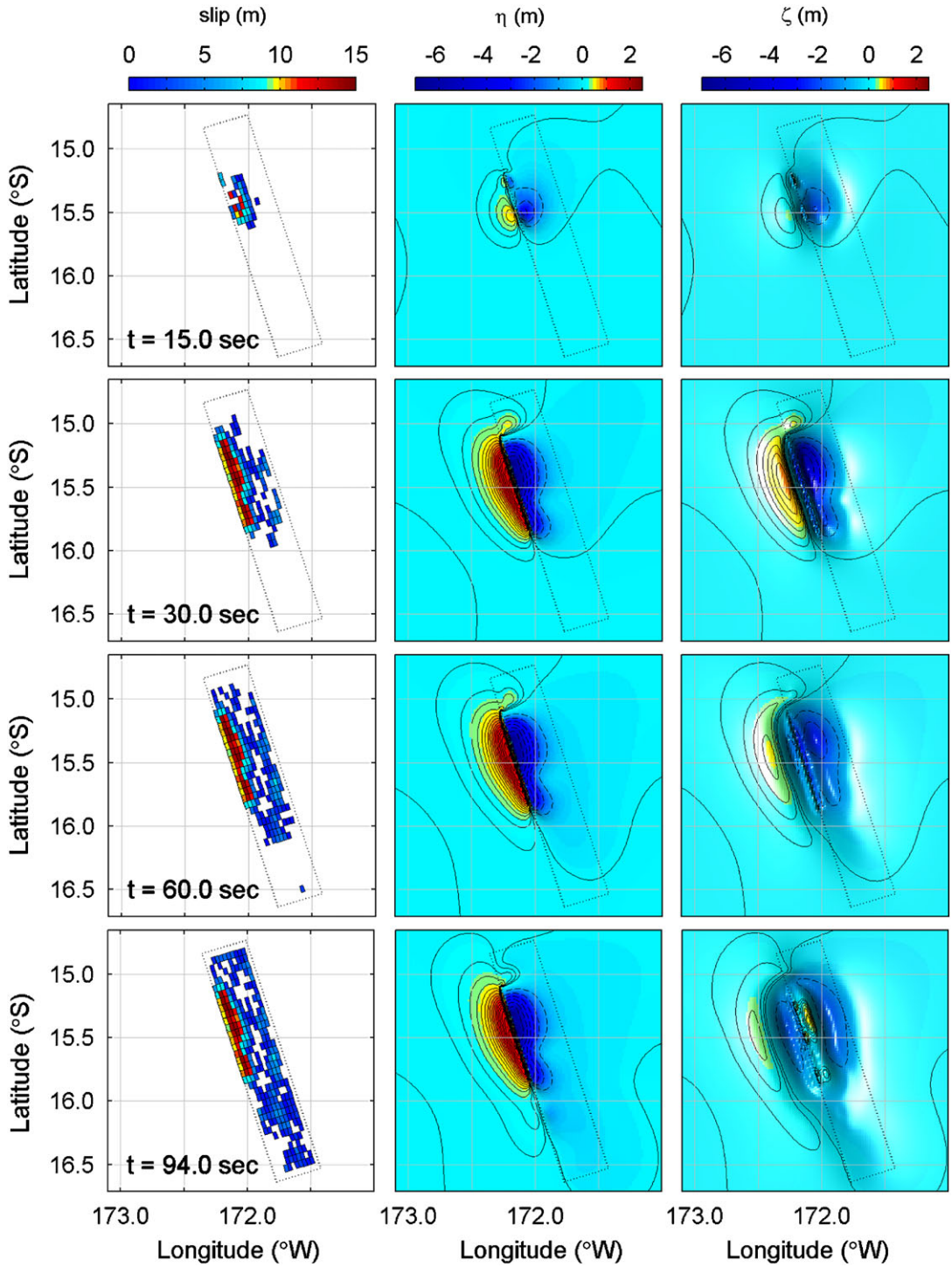

Figure 12. Time sequence of rupture, seafloor deformation, and surface elevation. ——, uplift contours at 0.2 m intervals; - - - -, subsidence contours at 1.0 m intervals; ..... (white), rupture area.

seafloor. The vertical displacement transfers both the kinetic and potential energy to the water. The generation of tsunami waves occurs simultaneously with the propagation of the energy away from the source. These dynamic processes result in different seafloor deformation and surface wave patterns in contrast to the static deformation approach commonly used in tsunami modeling.

DOI: 10.1002/fld

The earthquake releases most of the energy in 30 s and the subsequent rupture has minimal effect on the seafloor deformation. By the end of the rupture at $t = 94$ s, the tsunami has propagated over a considerable distance with a leading depression toward the Samoa Islands.

5.3. *Surface elevation and run-up*

Tsunami energy propagation is directional with the majority perpendicular to the fault line. Figure 13 shows the tsunami wave amplitude over South Central Pacific with a maximum value of 1.8 m over the deep ocean. The main energy propagates toward Tonga and American Samoa, where the tide gauge in Pago Pago Harbor recorded a strong signal of the tsunami. The three DART buoys, which are located roughly along the strike direction off the main energy beams, also recorded clear signals.

Pago Pago Harbor is an L-shape embayment with fringing reefs along its shores. The reefs converge at the west end of the harbor forming an extended shallow flat favorable to bore and hydraulic jump formation [44]. The water over the 1000-m long reef flat is approximately 10 m deep and the depth increases to 30 m over a distance of 500 m from the reef edge. Figure 14 shows a series of the computed surface elevation in the inner harbor that corroborates eyewitness accounts during the first wave [38]. The water begins to withdraw approximately 20 min after the earthquake exposing the shallow reef flats along the shores. The first positive wave, which arrives shortly afterward, reaches a surface elevation of 2 m in the inner harbor and floods the low-lying coastal areas on the north and south sides. The wave develops a sharp surface gradient over the reef flat around $t = 26$ min and transforms into a surge as it hits dry land reaching a maximum elevation of 8.14 m and producing extensive damage in the area. A hydraulic jump develops at the reef edge around $t = 31.0$ min as the floodwater returns to the harbor. The wave retreats faster than the receding floodwater resulting in accumulation of water on land and a waterfall over the reef edge until the next wave arrives.

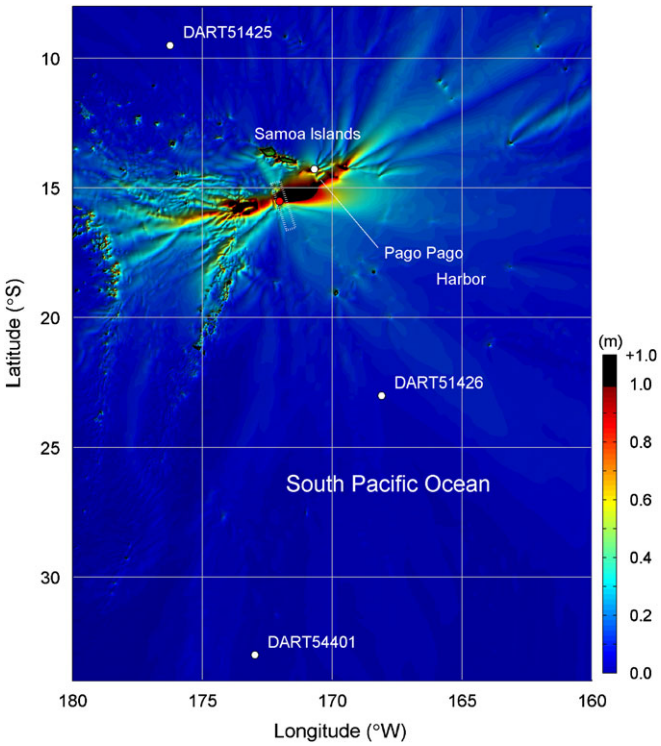

Figure 13. Computed maximum surface elevation of the 2009 Samoa Tsunami. ○ (white), water level stations; ○ (red), epicenter of the 2009 Samoa Earthquake; ..... (white), rupture area.

DOI: 10.1002/fld

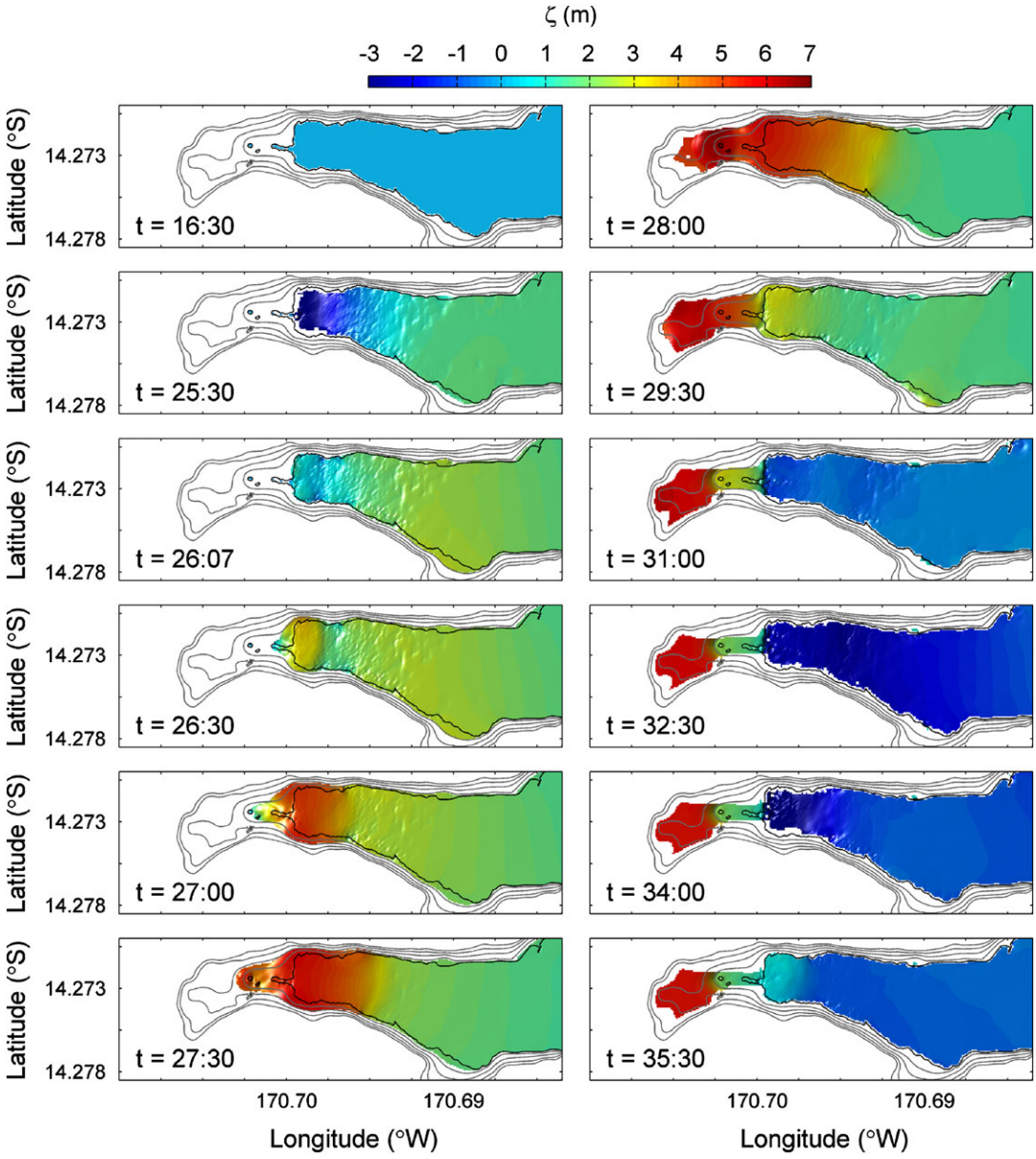

Figure 14. Wave propagation and inundation at inner Pago Pago Harbor. —— (black), coastline; —— (gray), contours at 2.5 m intervals.

Figure 15 shows a comparison of the recorded and computed waveforms and spectra at the Pago Pago tide gauge and the three DART buoys. The computed results show good agreement of the arrival time, amplitude, and frequency content with the measurements. The model reproduces the initial negative wave at the tide gauge and captures the distinct 11- and 18-min oscillations at Pago Pago Harbor. Some discrepancies of the initial waveforms are evident at the DART buoys. The model overestimates the amplitude of the leading depression at DART 51425 and cannot describe the polarity at DART 51426 and 54401. However, the amplitude recorded at these buoys is less than 4% of the 1.8 m maximum amplitude in the open ocean to the east of the source. The discrepancy is likely due to a secondary rupture in the forearc recently reported by Lay *et al.* [45]. The primary source mechanism from the USGS finite fault solution is deemed accurate as it reproduces the observations and strong tsunami signals at Pago Pago Harbor. In fact, the model results at DART

DOI: 10.1002/fld

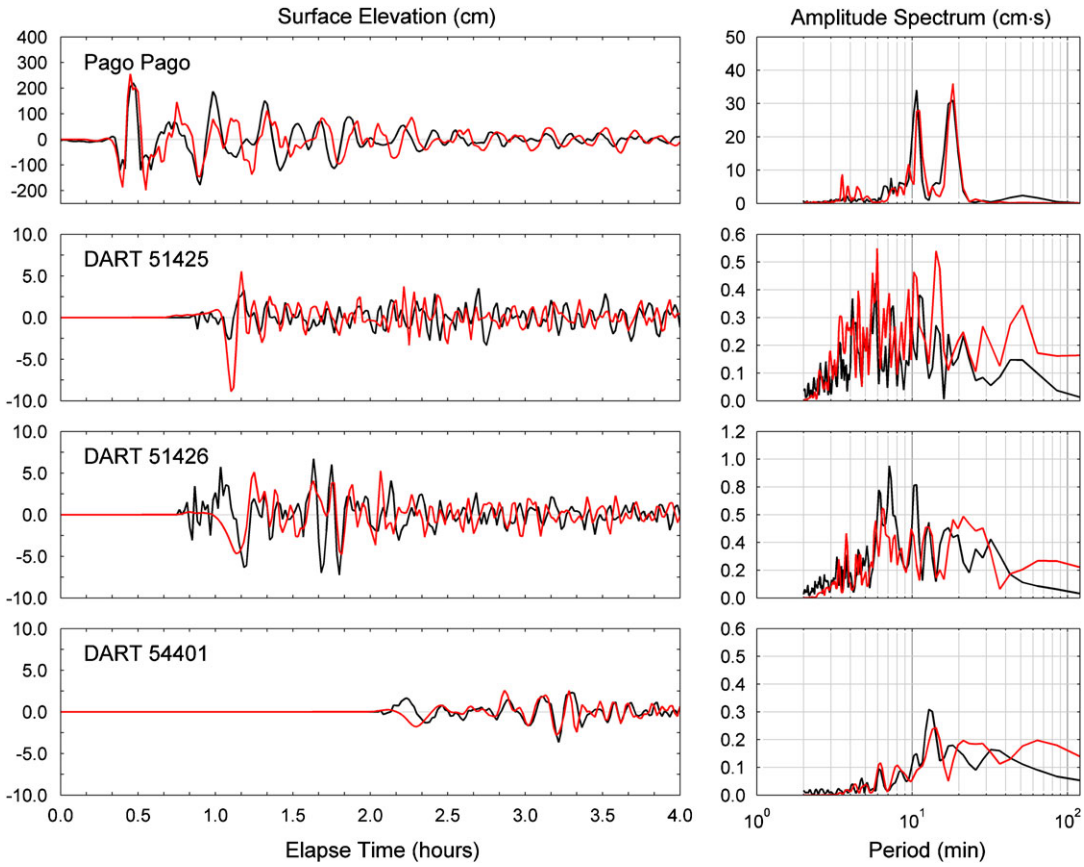

Figure 15. Time series and spectra of surface elevations at water level stations. —— (black), recorded data; —— (red), computed data.

51426 and 54401 reproduce the high-amplitude reflected waves from Tutuila arriving at 1.6 and 3.2 h after the earthquake.

Pago Pago Harbor is approximately 50 m deep, while the 100-m deep outside embayment is sheltered by barrier reefs along the edge of the insular shelf as shown in Figure 16(a). The configuration of the harbor and embayment is prone to trapping of long waves and the two distinct peaks in the amplitude spectrum are indicative of resonance. Following the method of Munger and Cheung [46] based on Fast Fourier Transform, we extract the oscillation modes of the modeled tsunami waves to understand the resonance characteristics. The spectral analysis depicts three resonance modes at 9.7, 11, and 18 min period in Pago Pago Harbor that are plotted in Figures 16(b)–(d). The first resonance at 18 min extends from the embayment into Pago Pago Harbor. The resonance mode shows a node over the insular shelf and an antinode at the tip of the harbor. The second resonance mode at 11 min covers the same region with nodes at the harbor entrance and the edge of the insular shelf. The third mode at 9.7 min, with a relatively lower energy level in this event, has an additional node in the outside embayment. The combined effect of the first two resonance modes provides an explanation for the significant inundation and property damage despite the well-sheltered location of the inner harbor.

The results presented so far have been based on the smoothed bathymetry in Figure 10(b). We compute the run-up and inundation at the level-4 grid with both the smoothed and original bathymetry to assess the effectiveness of the depth-dependent smoothing scheme. Figure 17 compares the computed run-up and inundation around Pago Pago Harbor with the measurements from Koshimura *et al.* [38] and Okal *et al.* [40]. The two sets of computed run-up results are almost identical thereby verifying the proposed smoothing scheme that serves to improve model

DOI: 10.1002/fld

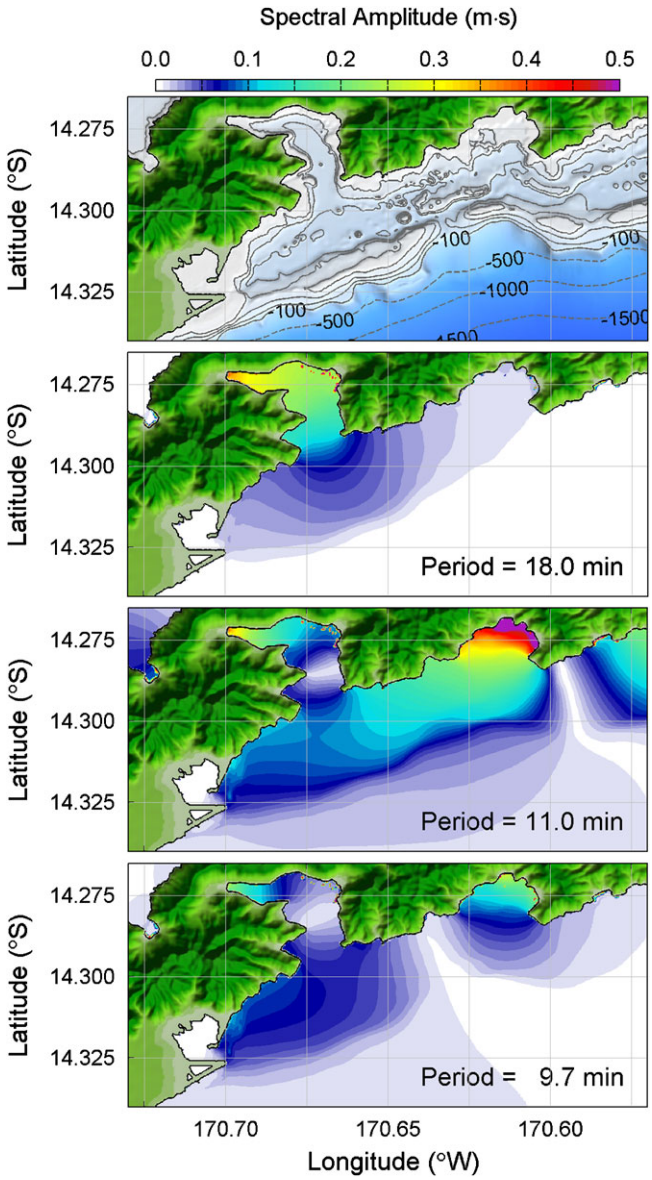

Figure 16. Detailed bathymetry and resonance modes around Pago Pago Harbor: (a) bathymetry; (b) first mode at 18 min; (c) second mode at 11 min; and (d) third mode at 9.6 min. —— (grey), depth contours at 25 m intervals; - - - - (gray), depth contours at 500 m intervals.

convergence without appreciable alteration of the model results. The smoothing of the bathymetry results in a 10% reduction on the number of iterations in the non-hydrostatic solver that is relatively minor because of the lack of small-scale, steep bottom features in the level-4 grid. In some situations, smoothing is necessary to obtain converging non-hydrostatic solutions. The model reproduces the overall pattern and height of the run-up along the coast. The minor discrepancies between the computed results and the measurements are primarily due to errors in the topographic data and the difficulties in modeling inundation in the built environment around Pago Pago Harbor. The large run-up at the tip and low values in the outer harbor show strong correlation with the three resonance modes. Such oscillations, which extend over the entire insular shelf and slope, provide an explanation for the local amplification and the disparate property damage along the coastlines of Tutuila [47].

DOI: 10.1002/fld

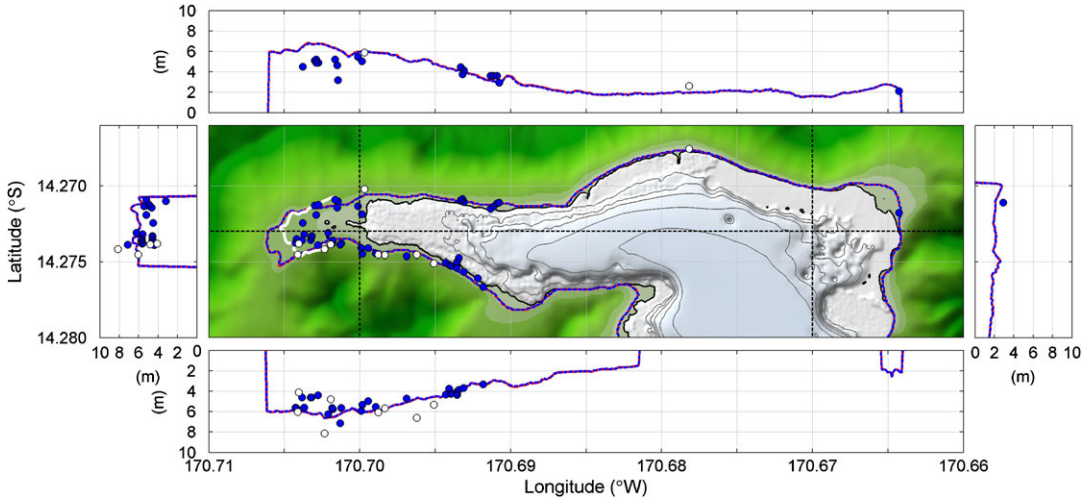

Figure 17. Run-up and inundation at inner Pago Pago Harbor. —— (white), recorded inundation; ○ (white), recorded run-up; ○ (blue), recorded flow depth plus land elevation; —— (red), solution with smoothed bathymetry; - - - - (blue), solution with non-smoothed bathymetry; —— (black), coastline; —— (gray), depth contours at 10 m intervals.

6. CONCLUSIONS AND FUTURE WORK

This paper has demonstrated the versatility and robustness of a depth-integrated, non-hydrostatic model for tsunami research and impact assessment. The inclusion of the non-hydrostatic pressure and vertical velocity in the governing equations allows modeling of dynamic seafloor deformation in tsunami generation and wave dispersion effects during the evolution processes. The formulation in the spherical coordinate system accounts for the earth's curvature in basin-wide tsunami propagation and yet is flexible enough to model inundation at a regional scale. Implementation of the momentum-conserved advection scheme with an upwind flux approximation allows modeling of flow discontinuities associated with bores and hydraulic jumps during the run-up and drawdown process.

The lower order spatial derivatives in the governing equations facilitate implementation of a grid-nesting scheme for the shock-capturing, dispersive wave model. A two-way nesting scheme exchanges the horizontal velocity, surface elevation, and non-hydrostatic pressure between an inner and an outer grid at every outer grid time step. The use of both the velocity and surface elevation in the nesting scheme is necessary for the momentum-conserved advection scheme, the upwind flux approximation, and computation of Coriolis effects. A Dirichlet boundary condition of the non-hydrostatic pressure ensures that wave dispersion is continuous across inter-grid boundaries. This grid nesting scheme enables the use of non-rectangular computational domains that can adapt to depth contours and bathymetric features for optimization of computational time.

Numerical experiments of solitary wave propagation in a channel and N-wave run-up in Monai Valley verify the proposed grid-nesting scheme. The present model is applied to reconstruct the 2009 Samoa Tsunami from the USGS finite fault solution. The model reproduces resonance and flow discontinuities and provides an explanation of the observed tsunami behaviors and impacts in Pago Pago Harbor. The computed surface elevations at the DART buoys and the Pago Pago Harbor tide gauge as well as the run-up around the harbor show very good agreement with recorded data. The depth-dependent smoothing scheme improves computational efficiency without noticeable modification of the computed water level and run-up. The case study demonstrates the capability of the present model in describing generation, propagation, and run-up of real-field tsunamis.

This paper has described an alternate direction in tsunami modeling with ample opportunities for research and development. These include enhancement of the dispersion characteristics for modeling of coastal processes, parallelization for improvement of computational efficiency,

DOI: 10.1002/fld

extension to include horizontal seafloor deformation, and coupling with a three-dimensional hydrodynamics model for landslide-generated tsunamis. On-going and future applications include tsunami inundation mapping for Hawaii, American Samoa, the US Gulf coasts, and Chile as well as paleotsunami modeling and impact assessment for Western Samoa. The present theoretical and numerical formulations, which build on the nonlinear shallow-water equations, can be implemented in most commonly used long-wave models.

ACKNOWLEDGEMENTS

This publication is funded in part by a grant/cooperative agreement from the National Oceanic and Atmospheric Administration (NOAA), Project No. R/IR-2, which is sponsored by the University of Hawaii Sea Grant College Program, School of Ocean and Earth Science and Technology (SOEST), under Institutional Grant No. NA05OAR4171048 from NOAA Office of Sea Grant, Department of Commerce. The National Tsunami Hazard Mitigation Program and Hawaii State Civil Defense provided additional support through the project 'Tsunami Inundation Map for Hawaii'. The authors thank Dr Juan Horrillo, Mr William Knight, and Dr Tokihiro Katsui for their input to the model development, Dr Masafumi Matsuyama for providing the input and recorded data of the Monai Valley experiment, Dr Gavin Hayes for supplying the finite fault solution of the 2009 Samoa Earthquake, and Dr Hermann Fritz and Dr Shunichi Koshimura for providing the recorded run-up and inundation data of the 2009 Samoa Tsunami around Pago Pago Harbor. The views expressed herein are those of the authors and do not necessarily reflect the views of NOAA and any of its subagencies. UNIHI-SEAGRANT-JC-09-35. SOEST Contribution No. 8000.

REFERENCES

1. Shuto N, Goto C. Numerical simulation of tsunami run-up. *Coastal Engineering in Japan* 1978; **21**(1):13–20.
2. Mader CL, Curtis G. Modeling Hilo, Hawaii tsunami inundation. *Science of Tsunami Hazards* 1991; **9**(1):85–94.
3. Kowalik Z, Murty TS. *Numerical Modeling of Ocean Dynamics*. World Scientific: Singapore, 1993.
4. Imamura F. Review of tsunami simulation with a finite difference method. In *Long-wave Runup Models*, Yeh H, Liu P, Synolakis C (eds). World Scientific: Singapore, 1996; 25–42.
5. Liu PLF, Cho YS, Yoon SB, Seo SN. Numerical simulations of the 1960 Chilean Tsunami propagation and inundation at Hilo, Hawaii. In *Tsunami*: *Progress in Prediction*, *Disaster Prevention and Warning*, Tsuchiya Y, Shuto N (eds). Kluwer Academic Publishers: Dordrecht, 1995; 99–116.
6. Goto C, Ogawa Y, Shuto N, Imamura. IUGG/IOC time project: numerical method of tsunami simulation with the leap-frog scheme. *Manuals and Guides*, no. 35, Intergovernmental Oceanographic Commission of UNESCO, Paris, 1997.
7. Titov VV, Synolakis CE. Numerical modeling of tidal wave runup. *Journal of Waterway*, *Port*, *Coastal*, *and Ocean Engineering* 1998; **124**(4):157–171.
8. Wei Y, Cheung KF, Curtis GD, McCreery CS. Inverse algorithm for tsunami forecasts. *Journal of Waterway*, *Port*, *Coastal*, *and Ocean Engineering* 2003; **129**(2):60–69.
9. Kajiura K. Tsunami source, energy and the directivity of wave radiation. *Bulletin of Earthquake Research Institute* 1970; **48**:835–869.
10. Ohmachi T, Tsukiyama H, Matsumoto H. Simulation of tsunami induced by dynamic displacement of seabed due to seismic faulting. *Bulletin of the Seismological Society of America* 2001; **91**(6):1898–1909.
11. Horrillo J, Kowalik Z, Shigihara Y. Wave dispersion study in the Indian Ocean tsunami of December 26, 2004. *Marine Geodesy* 2006; **29**(1):149–166.
12. Wei Y, Mao XZ, Cheung KF. Well-balanced finite-volume model for long-wave runup. *Journal of Waterway*, *Port*, *Coastal*, *and Ocean Engineering* 2006; **132**(2):114–124.
13. Song YT, Fu L-L, Zlotnicki V, Ji C, Hjorleifsdottir V, Shum CK, Yi Y. The role of horizontal impulses of the faulting continental slope in generating the 26 December 2004 tsunami. *Ocean Modelling* 2008; **20**(4):362–379.
14. Briggs MJ, Synolakis CE, Harkins GS, Green DR. Laboratory experiments of tsunami runup on a circular island. *Pure and Applied Geophysics* 1995; **144**(3/4):569–593.
15. Bricker JD, Munger S, Pequignet C, Wells JR, Pawlak G, Cheung KF. ADCP observations of edge waves off Oahu in the wake of the November 2006 Kuril Island Tsunami. *Geophysical Research Letters* 2007; **34**(23):L23617. DOI: 10.1029/2007GL032015.
16. Stelling GS, Zijlema M. An accurate and efficient finite-difference algorithm for non-hydrostatic free-surface flow with application to wave propagation. *International Journal for Numerical Methods in Fluids* 2003; **43**(1):1–23.
17. Yamazaki Y, Kowalik Z, Cheung KF. Depth-integrated, non-hydrostatic model for wave breaking and run-up. *International Journal for Numerical Methods in Fluids* 2009; **61**(5):473–497.
18. Dodd N. Numerical model of wave run-up, overtopping, and regeneration. *Journal of Waterway*, *Port*, *Coastal and Ocean Engineering* 1998; **124**(2):73–81.

DOI: 10.1002/fld

19. Zhou JG, Causon DM, Mingham CG, Ingram DM. The surface gradient method for the treatment of source terms in the shallow-water equations. *Journal of Computational Physics* 2001; **168**(1):1–25.
20. Wu YY, Cheung KF. Explicit solution to the exact Riemann problem and application in nonlinear shallow-water equations. *International Journal for Numerical Methods in Fluids* 2008; **57**(11):1649–1668.
21. Stelling GS, Duinmeijer SPA. A staggered conservative scheme for every Froude number in rapidly varied shallow water flows. *International Journal for Numerical Methods in Fluids* 2003; **43**(12):1329–1354.
22. Zijlema M, Stelling GS. Efficient computation of surf zone waves using the nonlinear shallow water equations with non-hydrostatic pressure. *Coastal Engineering* 2008; **55**(10):780–790.
23. Honda R, Soi S, Morioka N, Sekiguchi H, Kunugi T, Fujiwara H. Ground motion and rupture process of the 2003 Tokachi-Oki earthquake obtained by strong motion data of K-NET and KiK-net. *Earth Planets Space* 2004; **56**(3):317–322.
24. Ji C, Wald DJ, Hemberger DV. Source description of the 1999 Hector Mine, California, Earthquake. Part I: wavelet domain inversion theory and resolution analysis. *Bulletin of the Seismological Society of America* 2002; **92**(4):1192–1207.
25. Matsuyama M, Tanaka H. An experimental study of the highest run-up height in the 1993 Hokkaido Nansei-Oki earthquake tsunami. *Proceedings of the International Tsunami Symposium 2001*, Session 7, Seattle, WA, 7–10 August 2001; 879–889.
26. Løvholt F, Pederson G. Instabilities of Boussinesq models in non-uniform depth. *International Journal for Numerical Methods in Fluids* 2008; **61**(6):606–637.
27. Mader CL. *Numerical Modeling of Water Waves*. University of California Press: California, 1988.
28. Kowalik Z, Knight W, Logan T, Whitmore P. Numerical modeling of the global tsunami: Indonesian Tsunami of 26 December 2004. *Science of Tsunami Hazards* 2005; **23**(1):40–56.
29. Gill AL. *Atmosphere-Ocean Dynamics*. Academic Press: London, 1982.
30. Casulli V. A semi-implicit finite difference method for non-hydrostatic free surface flows. *International Journal for Numerical Methods in Fluids* 1999; **30**(4):425–440.
31. Stone HL. Iterative solution of implicit approximations of multidimensional partial differential equations. *SIAM Journal on Numerical Analysis* 1968; **5**(3):530–558.
32. Park KY, Borthwick AGL. Quadtree grid numerical model of nearshore wave-current interaction. *Coastal Engineering* 2001; **42**(3):219–239.
33. George DL. Adaptive finite volume methods with well-balanced Riemann solvers for modeling floods in rugged terrain: application to the Malpasset dam-break flood (France, 1959). *International Journal for Numerical Methods in Fluids* 2010; DOI: 10.1002/fld.2298.
34. Liang Q, Du G, Hall JW, Borthwick AGL. Flood inundation modeling with an adaptive quadtree grid shallow water equation solver. *Journal of Waterway*, *Port*, *Coastal and Ocean Engineering* 2008; **134**(11):1603–1610.
35. Plant NG, Edwards KL, Kaihatu JM, Veeramony J, Hsu L, Holland KT. The effect of bathymetry filtering on nearshore process model results. *Coastal Engineering* 2009; **56**(4):484–493.
36. Chaudhry MH. *Open-Channel Flow*. Prentice-Hall Inc.: Englewood Cliffs, NJ, 1993.
37. Bare AY, Grimshaw KL, Rooney JJ, Sabater MG, Fenner D, Carroll B. Mesophotic communities of the insular shelf at Tutuila, American Samoa. *Coral Reefs* 2010; **29**(2):369–377.
38. Koshimura S, Nishimura Y, Nakamura Y, Namegaya Y, Fryer GJ, Akapo A, Kong LS, Vargo D. Field survey of the 2009 tsunami in American Samoa. *EOS Transactions of the American Geophysical Union* **90**(52), Fall Meeting Supplemental Abstract U23F-07, 2009.
39. Jaffe BE, Gelfenbaum G, Buckley ML, Watt S, Apotsos A, Stevens AW, Richmond BM. The limit of inundation of the September 29, 2009, tsunami on Tutuila, American Samoa. *US Geological Survey Open-File Report 2010-1018*, U.S. Geological Survey, 2010.
40. Okal EA, Fritz HM, Synolakis CE, Borrero JC, Weiss R, Lynett PJ, Titov VV, Foteinis S, Jaffe BE, Liu PLF, Chan IC. Filed survey of the Samoa Tsunami on 29 September 2009. *Seismological Society of America* 2010; **81**(4):577–591.
41. Bretschneider CL, Krock HJ, Nakazaki E, Casciano FM. Roughness of typical Hawaiian terrain for tsunami run-up calculations: a user's manual. *J.K.K. Look Laboratory Report*, University of Hawaii, Honolulu, HI, 1986.
42. Okada Y. Surface deformation due to shear and tensile faults in a half space. *Bulletin of the Seismological Society of America* 2009; **75**(4):1135–1154.
43. Irikura K. Semi-empirical estimation of strong ground motions during large earthquakes. *Bulletin of the Disaster Prevention Research Institute* 1983; **33–2**(298):63–104.
44. Roeber V, Cheung KF, Kobayashi MH. Shock-capturing Boussinesq-type model for nearshore wave processes. *Coastal Engineering* 2010; **57**(4):407–423.
45. Lay T, Ammon CJ, Kanamori H, Rivera L, Koper K, Hutko A. The 2009 Samoa–Tonga great earthquake triggered doublet. *Nature* 2010; **466**(7309):964–968.
46. Munger S, Cheung KF. Resonance in Hawaii waters from the 2006 Kuril Islands Tsunami. *Geophysical Research Letters* 2008; **35**(7):L07605. DOI: 10.1029/2007GL032843.
47. Roeber V, Yamazaki Y, Cheung KF. Resonance and impact of the 2009 Samoa tsunami around Tutuila, American Samoa. *Geophysical Research Letters* 2010; **37**:L21604. DOI: 10.1029/2010GL044419.